Basin Research

RESEARCH ARTICLE OPEN ACCESS

Sand Injectites

Provenance and Petrological Evolution of Sand Injection Complexes: Insights From Heavy Mineral Analysis in the Paleogene Forearc Succession of the San Joaquin Basin

Gustavo Zvirtes[1] | Andrew Morton[1,2] | Andrew Hurst[1] | Ruy Paulo Philipp[1,3] | Wiktor Luzinski[1] | Giuseppe Palladino[1,4] | Luciano Alessandretti[5]

[1]Department of Geology and Geophysics, School of Geosciences, University of Aberdeen, Aberdeen, UK | [2]CASP, Cambridge, UK | [3]Departamento de Mineralogia e Petrologia, Universidade Federal do Rio Grande do Sul, Porto Alegre, Rio Grande do Sul, Brazil | [4]Dipartimento di Scienze di Base e Applicate (DISBA), Università degli Studi della Basilicata, Potenza, Italy | [5]Laboratório de Paleontologia Estratigráfica, Instituto de Geografia, Geociências e Saúde Coletiva, Universidade Federal de Uberlândia, Campus Monte Carmelo, Monte Carmelo, MG, Brazil

Correspondence: Gustavo Zvirtes (gustavo.zvirtes1@abdn.ac.uk)

Received: 3 April 2025 | **Revised:** 18 March 2026 | **Accepted:** 25 March 2026

Keywords: grain degradation | heavy minerals | hydraulic sorting | provenance | sand injection complexes | statistical analysis

ABSTRACT

The lithostratigraphy of sand injection complexes (SICs) is governed by the architectural and petrological relationships between depositional parent units and intrusive networks. During the formation and evolution of SICs, diverse geological processes can modify mineral assemblages and textures, offering opportunities to evaluate genetic mechanisms and support petrological correlations. This study integrates field mapping with heavy mineral analysis of the Paleogene succession in the San Joaquin Basin, specifically targeting the upper Eocene Tumey Giant Injection Complex (TGIC) to investigate provenance of depositional and intrusive sandstones and processes associated with injection emplacement. Statistical analysis of heavy mineral assemblages and provenance-sensitive indices (*MZi*, *GZi*, *CZi* and *RZi*) confirms the genetic link between the slope channel-fills of the Kreyenhagen Formation and sandstone intrusions. These assemblages indicate derivation from granitic and metasedimentary sources derived from the Sierra Nevada Province to the east. In contrast, the underlying shallow-marine Domengine Formation reveals mixed sourcing, with significant blueschist-facies minerals (lawsonite and glaucophane) likely supplied by the Franciscan Complex accretionary prism to the west. While low ZTR values in the parent channel-fills and most intrusions indicate mineralogical immaturity, specific intrusive facies exhibit high ZTR and low ATi, suggesting mechanical degradation of less durable grains during sand injection. Qualitative grain morphology analysis reinforces this, showing a higher degree of grain damage within intrusions in comparison to parent unit. Furthermore, density-controlled ZTi index reveals hydraulic segregation, evidenced by the progressive settling of denser zircon grains through a km-scale wing-like intrusion. The petrological signature of the TGIC is thus a function of parent unit composition, intra-granular mechanical interaction, and hydraulic sorting under dynamic fluid-flow conditions. Despite the inherent 3D architectural complexity of the intrusive networks, this study provides robust methodological tools for investigating the evolution of injectites in diverse geodynamic settings.

1 | Introduction

Sand injection complexes (SICs) illustrate the dynamic nature of sedimentary basins by promoting extensive sand remobilization and injection (> 100 s km^3) into the shallow crust (< 1.5 km depths) (Hurst et al. 2011; Vigorito et al. 2022). Documented across diverse geodynamic and geological settings and scales, SICs are mostly assumed to be formed through a combination

---

Highlights

- Heavy mineral assemblages constrain provenance signatures of Paleogene depositional and intrusive sandstones.
- Detrital signatures reveal dual sourcing from Sierra Nevada and Franciscan Complex.
- Multivariate statistical analysis attests the Kreyenhagen slope channel-fills as parent units.
- Grain degradation during sand injection suggested by *ZTR* and *ATi* values.
- Variations in *ZTi* indicate density-driven hydraulic sorting during sediment remobilization and injection.

of processes that induce overpressure conditions, seal failure via hydrofracturing of low-permeability strata (e.g., mudstone), followed by sediment fluidization and remobilization of buried sand deposits (parent units) and forceful injection into host units (Duranti and Hurst 2004; Cartwright et al. 2007; Vigorito and Hurst 2010; Andrews et al. 2026, and references herein). The resulting intrusive networks, commonly comprising dykes, sills, breccias and other irregular bodies, can extend laterally for kilometres and vertically penetrate hundreds of meters of strata (Scott et al. 2013; Grippa et al. 2019, Zvirtes et al. 2019). Therefore, the development of SICs effectively reactivates sediment transport, remobilizing sand from buried sinks into intrusive networks. These often extend upward into shallower sections or, in the case of extrudites, reach the seafloor (Figure 1).

The lithostratigraphic analysis of SICs relies on identifying the genetic relationships between three key components: (1) *Parent units*: buried, unconsolidated sandy depositional bodies deformed by sand fluidization and remobilization; (2) *Intrusive network*: sandstone dykes, sills, wings, saucers, injection breccias and other irregular bodies fed by parent units; and (3) *Extrudite*s: extrusive deposits onto the free surface, fed by the underlying parent units and intrusive network (Hurst et al. 2006). Although these components often share similar petrological characteristics, syn- and post-injection processes are reported to be responsible for influencing mineral assemblages and textures (Scott et al. 2009, 2013; Hurst et al. 2017, 2021; Zvirtes et al. 2019, 2020; Luzinski et al. 2022). While these changes may complicate direct lithostratigraphic correlations and lead to ambiguous interpretations, they also introduce distinct compositional trends and features that can serve as diagnostic markers for identification of injectites and the processes responsible for their development.

Despite their geological significance, petrological characterizations of SICs remain limited. Consequently, our understanding of the complex interplay between sediment fluidization, injection dynamics, and subsequent post-emplacement processes is still in its infancy. In depositional systems, the composition and texture of sediments are influenced by both external and internal controls, including: (1) tectonic setting; (2) climate; (3) lithology of source rocks; (4) sediment erosion and production from source areas; (5) sediment transport and transit trajectories from source to sink; (6) physical and chemical properties of minerals, such as grain density, size, shape, and mechanical and chemical stability; (7) depositional environments; (8) diagenesis; and (9) weathering processes (Morton and Hallsworth 1994, 1999; Allen 2008; Weltje and von Eynatten 2004; Caracciolo 2020) (Figure 1). However, in sedimentary systems containing SICs, processes associated with sediment fluidization and injection along with post-emplacement diagenesis and weathering can also play a role in the final composition and texture of sandstones (Jonk 2010; Zvirtes et al. 2020; Hurst et al. 2021) (Figures 1 and 2). As such, these additional processes must be integrated into the sedimentological and petrological analysis to achieve a comprehensive understanding of the geological history of injectites (Figures 1 and 2).

Although regionally extensive outcrops of SICs are less frequently reported than subsurface examples, they provide exceptional opportunities for developing robust geological models through integrated stratigraphic, structural, and petrological studies, supporting subsurface interpretations (Scott et al. 2013; Cobain et al. 2015, 2017; Ravier et al. 2015; Hurst et al. 2017; Palladino et al. 2018, 2020; Grippa et al. 2019; Zvirtes et al. 2019; Waltham et al. 2024; Andrews et al. 2026). For this reason, this research applied heavy mineral analysis (HMA) in the Tumey Giant Injection Complex (TGIC) to investigate the evolution of SICs and the geological processes associated to their development and how these processes impact sandstone composition and textures. HMA is widely recognized as one of the most effective methods for determining sedimentary-rock provenance, reconstructing paleoenvironments, analysing hydrodynamic processes, and correlating facies to characterize the lithostratigraphy of sedimentary successions (A. C. Morton 1985; Mange-Rajetzky 1995; Morton and Hurst 1995; Mange and Wright 2007; and references herein). Therefore, HMA applied in the Paleogene succession of the San Joaquin Basin serves as a critical tool for reconstructing sediment dispersal patterns, defining the genesis of sandstone intrusions, and providing insights into compositional and textural characteristics through SICs development.

2 | Geological Setting

The TGIC crops out over an area $>100\,\mathrm{km}^2$, along an NNW–SSE outcrop belt in the eastern margin of the Diablo Range in central California (Figure 3). The complex consists of an interconnected network of parent units and sandstone intrusions developed within deep-marine slope succession of the Kreyenhagen Formation (middle-upper Eocene) in the San Joaquin Basin (Palladino et al. 2016; Zvirtes et al. 2019; Vigorito et al. 2024). Analysis of unpublished subsurface, seismic and well data indicates that the TGIC can extend over a much larger area, estimated at $>12{,}000\,\mathrm{km}^2$ within the Eocene succession of the basin.

The San Joaquin basin developed in a divergent tectonic setting that initiated in the latest Jurassic as the Farallon oceanic plate subducted under the North American continental plate (Atwater 1970; Dickinson and Seely 1979). This process resulted in the development of the Great Valley forearc basin system along with the Sierran magmatic arc to the east of the basin and the accretionary prism of the Franciscan Complex to the west (R. V. Ingersoll 1978, 1979; Wakabayashi 2015). Provenance

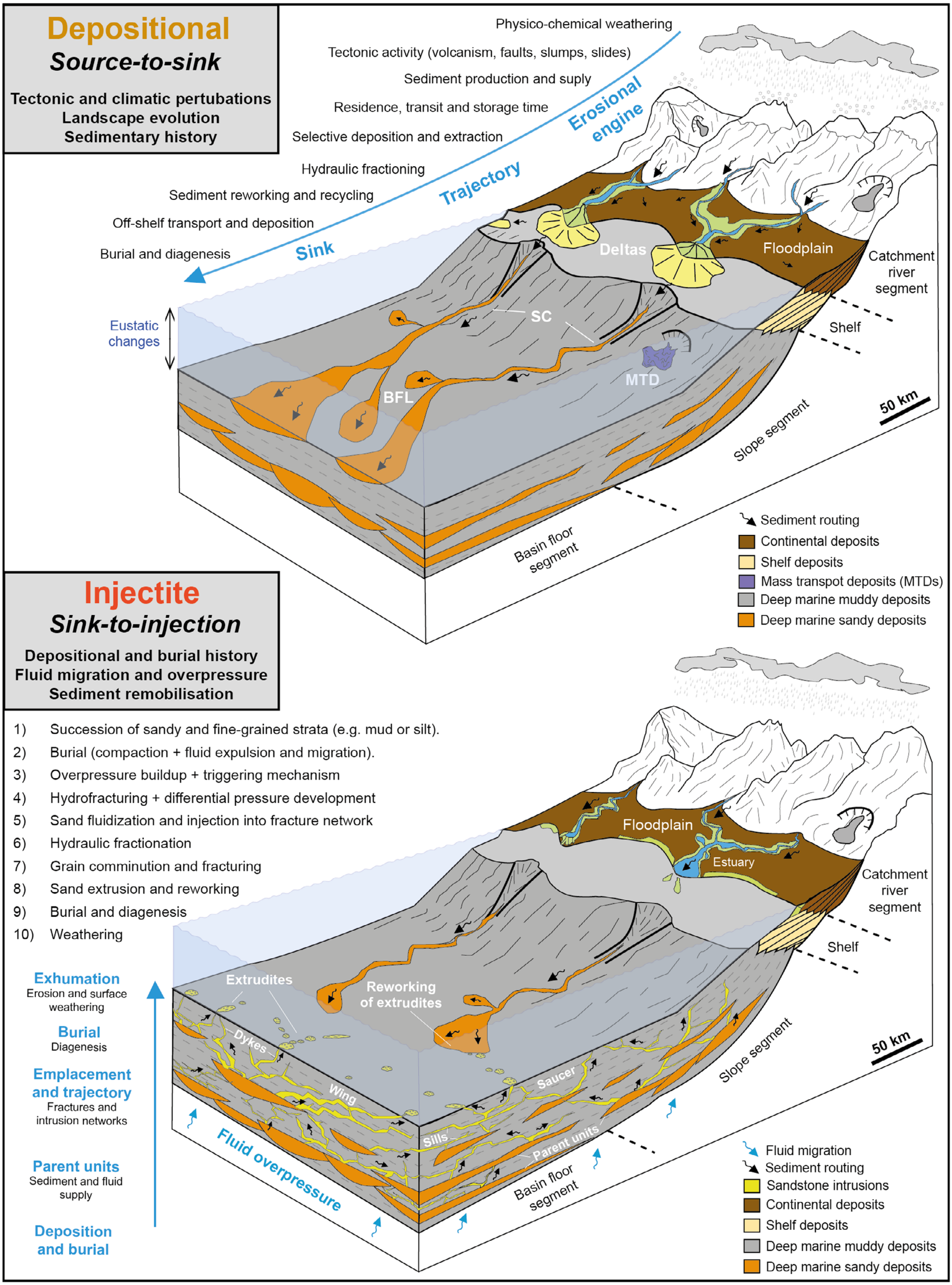

FIGURE 1 | Legend on next page.

FIGURE 1 | Schematic representation of main processes controlling composition and textures of sediments and rocks associated with depositional systems (top) and sand injection complexes (bottom). Processes associated with depositional systems were compiled from Morton and Hallsworth (1994) and Caracciolo (2020). The palaeogeography expresses the context of the deep marine depo-system associated to the Kreyenhagen Formation from middle to upper Eocene. SC, slope channels; BFL, basin floor lobes; MTD, Mass-transport deposits.

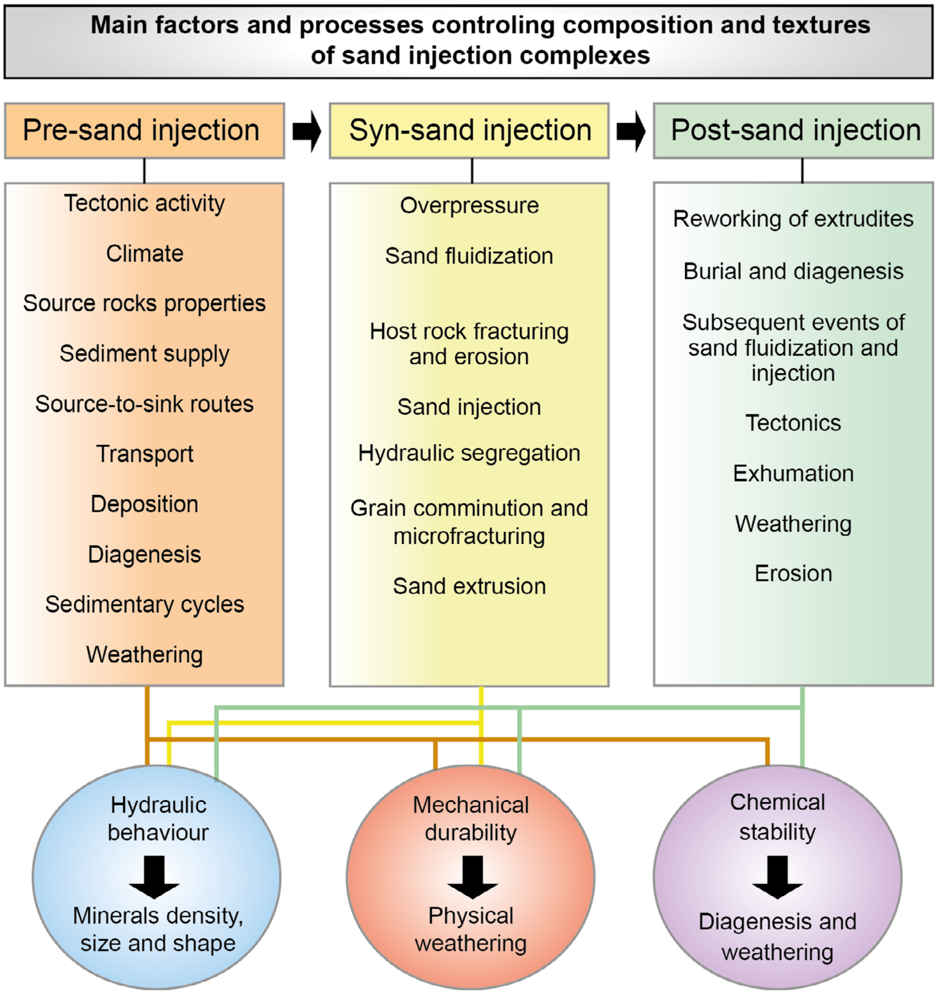

FIGURE 2 | Main processes, mechanisms and physical parameters controlling composition and textural variations of sandstones associated with sand injection complexes.

analyses (e.g., Dickinson and Rich 1972; R. V. Ingersoll 1983, 2012), bulk-rock geochemistry (Linn et al. 1992), and detrital-zircon geochronology (e.g., DeGraaff-Surpless et al. 2002; Sharman et al. 2015) indicate that the Sierran magmatic arc was the primary source of clastic material deposited as extensive deep-marine channel-fills and fan systems throughout the basin evolution. The Franciscan Complex, which underwent progressive uplift throughout the Cretaceous–Paleogene, also contributed with detrital input (McGuire 1988; Schulein 1993; Unruh et al. 2007; Mitchell et al. 2010; Sharman et al. 2017).

Around the limit between Late Eocene and Oligocene, the convergent margin started the transition into a transform margin, today marked by NW-SE strike-slip faults of the San Andreas fault system (Dickinson and Seely 1979; Bird and Ingersoll 2022, and references therein). This transition has profoundly impacted the palaeogeography and relative positioning of the tectonic units of the continental margin as well as on the provenance and source-to-sink configurations. Important examples of this impact are the uplift of the accretionary prism of the Franciscan Complex to the west (Unruh et al. 2007) and the tectonic displacement of fragments of the Cretaceous batholith, the Salinian Block, which migrated north-westward for hundreds of km (some estimations indicate up to 500 km) through dextral slip (Suppe 1970; Graham 1978; Sharman et al. 2013; Bird and Ingersoll 2022).

The San Joaquin basin fill includes thick sequences of Cretaceous and Cenozoic strata controlled by tectonic activity and eustatic sea-level changes (Johnson and Graham 2007). This dynamic tectonic setting controlled the deep- to shallow-marine successions of the basin where two major sand injection complexes were developed: the Panoche Giant Injection Complex (PGIC) within the upper Cretaceous-Lower Paleogene succession (Vigorito et al. 2022) and the TGIC within the Eocene succession (Zvirtes et al. 2019) (Figure 3).

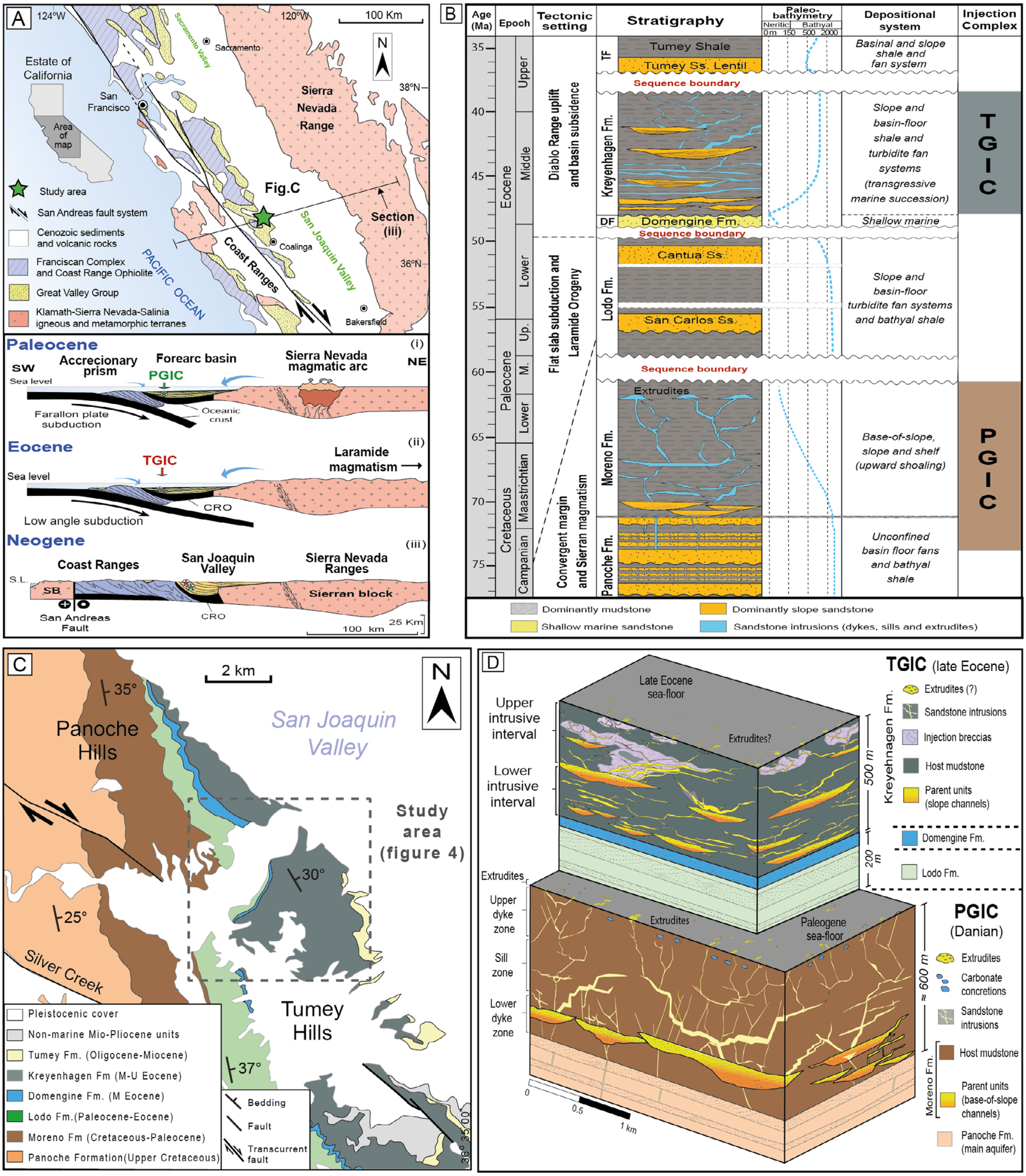

FIGURE 3 | (A) Geotectonic map of central California (top) and schematic representation of tectonic evolution from Cretaceous to present of the western North American margin (bottom) with relative position of Panoche Giant Injection Complex (PGIC) and Tumey Giant Injection Complex (TGIC). (B) Tectonic and stratigraphic column showing main tectonic events, stratigraphic sequences, depositional systems, and injection complexes. Adapted from Johnson and Graham (2007) and Sharman et al. (2017). (C) Regional geological map of the west margin of San Joaquin Valley and location of study area (dashed square). (D) Conceptual block diagram showing lithostratigraphy and architecture of the PGIC and TGIC.

The Danian PGIC formed within a basin floor, base-of-slope to shelf sequence represented by the Panoche and Moreno Formation (Payne 1951; McGuire 1988; Vigorito et al. 2022) (Figure 3C). A regional unconformity truncates the top of this sequence, which is overlain by slope-to-basin floor fans of the Lodo Formation (upper Palaeocene–lower Eocene) (Todd and Monroe 1968; Nilsen et al. 1974). During the middle Eocene, tectonic uplift and basin shoaling were marked by the development of a regional erosive unconformity, followed by deposition of transgressive shallow- to marginal-marine sediments of the Domengine Formation (Schulein 1993; Sullivan and Sullivan 2012; Sharman et al. 2017). Progressive basin-wide transgression associated with global sea-level rise and regional subsidence along the entire California margin led to the deposition of deep-marine slope succession of the Kreyenhagen Formation (Milam 1985; Moxon and Graham 1987; Bartow 1991) through which most of the TGIC developed. The formation consists of a widespread bathyal sequence dominated by calcareous, organic-rich, and siliceous mudstones that correspond to a major transgressive-regressive cycle with contemporaneous climatic cooling (Giannetta and Behl 2022). In the study area, this muddy succession is intercalated with stacked, amalgamated to isolated slope channel-fills and channel complexes, interpreted to be the main parent units of the TGIC (Zvirtes et al. 2019, Zvirtes et al. 2020).

The Kreyenhagen Formation and the TGIC are capped by a Late-Eocene unconformity which is erosively overlain by a broad submarine fan system of the Tumey Sandstone Lentil of the Tumey Formation (Zimmerman 1944; Scheirer and Magoon 2008).

2.1 | Architecture of the TGIC

The TGIC was formed by sand fluidization and remobilization from slope channel-fills of the Kreyenhagen Formation and coeval hydrofracturing and sand injection into host mudstones during the Late Eocene (Zvirtes et al. 2019; Vigorito et al. 2024). In the study area, there are two broad levels of channel-fills deposited by predominantly westward sediment gravity flows dominated by sandy debris flows and high-density turbidity currents (Figure 4). The intrusive network that emanates from the channel-fills consists of sandstone dykes, sills, injection breccias and other irregular bodies that extend laterally for tens of kilometres and intrude vertically > 450 m of clay-rich and biosiliceous mudstones. Individually these intrusive bodies can reach up to 15 m in thickness and in combination form architectural elements of sill complexes and wing-like intrusions.

Based on the distribution of parent units, intrusive geometries, facies associations, and host-rock composition, the TGIC was divided into lower and upper intrusive intervals by Zvirtes et al. (2019) (Figure 5). The lower interval (LII) is characterized by a 250 m thick succession of dark to light-brown clay-rich mudstone interbedded with isolated channel-fills (1–8 m thickness) and sheets (0.1–0.4 m thickness), and an intrusive network of sills (0.1–1.5 m thickness and tens of meters long) interconnected by shorter (0.1–10 m) and thinner (0.05–0.5 m) dykes. The upper intrusive interval (UII) is approximately 200 m thick and comprises mostly biosiliceous mudstones intercalated with channel-fills (up to 35 m thick). The main channel is directly connected to a kilometre-scale wing-like intrusion. The wing extends ca. 1.3 km laterally, cutting through ca. 200 m of host strata, consisting of interconnected stepped sill and dykes with individual intrusions reaching up to 15 m in thickness, and extensive injection breccia facies. The shallowest section (20–30 m thick) is dominated by thinner dykes and sills (0.05–0.5 m thick) along with injection breccias which are truncated by a Priabonian unconformity and overlain by Tumey Formation sandstones (Vigorito et al. 2024).

3 | Methods

Detailed geological mapping involved lithostratigraphic and structural analyses to assess the distribution and arrangement of depositional and intrusive sandstones. Twenty-six samples were collected for HMA, complemented by thin section descriptions. The sampling strategy included all major depositional units that could potentially serve as parent bodies to the complex, as well as intrusive sandstones from various intervals (Figure 4, Table 1). General information for all samples, including architectural elements, relative depths and geographic coordinates is reported in Table A1 of the Appendix.

Five samples were collected from depositional units underlying the TGIC: two fine-grained arkosic sandstones from deep marine fan of Lodo Formation and three fine-grained lithic arkoses from estuarine deposits of Domengine Formation. Twenty samples of fine- to medium-grained arkosic litharenites were collected from channel-fills of the Kreyenhagen Formation and intrusions throughout the complex.

In the LII, three samples from depositional channels and seven from intrusive sandstones (five sills and two dikes) were collected. In the UII, two samples from depositional sandstones and eight from intrusive sandstones (four dikes and four sills). In this interval, seven were systematically collected along a wing-like intrusion architecture to investigate compositional and textural variations. One sample from the overlying Tumey Sandstone Lentil was collected for stratigraphic contextualization.

The samples were preferentially collected from more homogeneous parts of the depositional units and central sections of intrusions to minimize hydraulic effects at the margins of the bodies. Samples between 300-500 g were disaggregated and cleaned using an ultrasonic probe, and wet sieved to capture the 63–125 μm grain size fraction (A. Morton 2012), thus reducing the effects of hydraulic sorting. Separation of heavy minerals was achieved by gravity-settling using bromoform (density: 2.89 g cm^{-3}). The relative abundance of minerals was determined through an optical microscope by a total of two hundred non-opaque detrital grains within each mount. Opaque minerals, diagenetic components, and minerals with anomalous hydrodynamic behaviour (mica and chlorite) were not included. A scanning electron microscope (ISI ABT-60 SEM) was used for imaging of grain microtextures.

3.1 | Heavy Mineral Indices

Various indices that utilize specific HM ratios to assess provenance of deposition and injected sandstones, compositional maturity, hydraulic fractionation processes, and pre- and post-depositional weathering were calculated using the formula below:

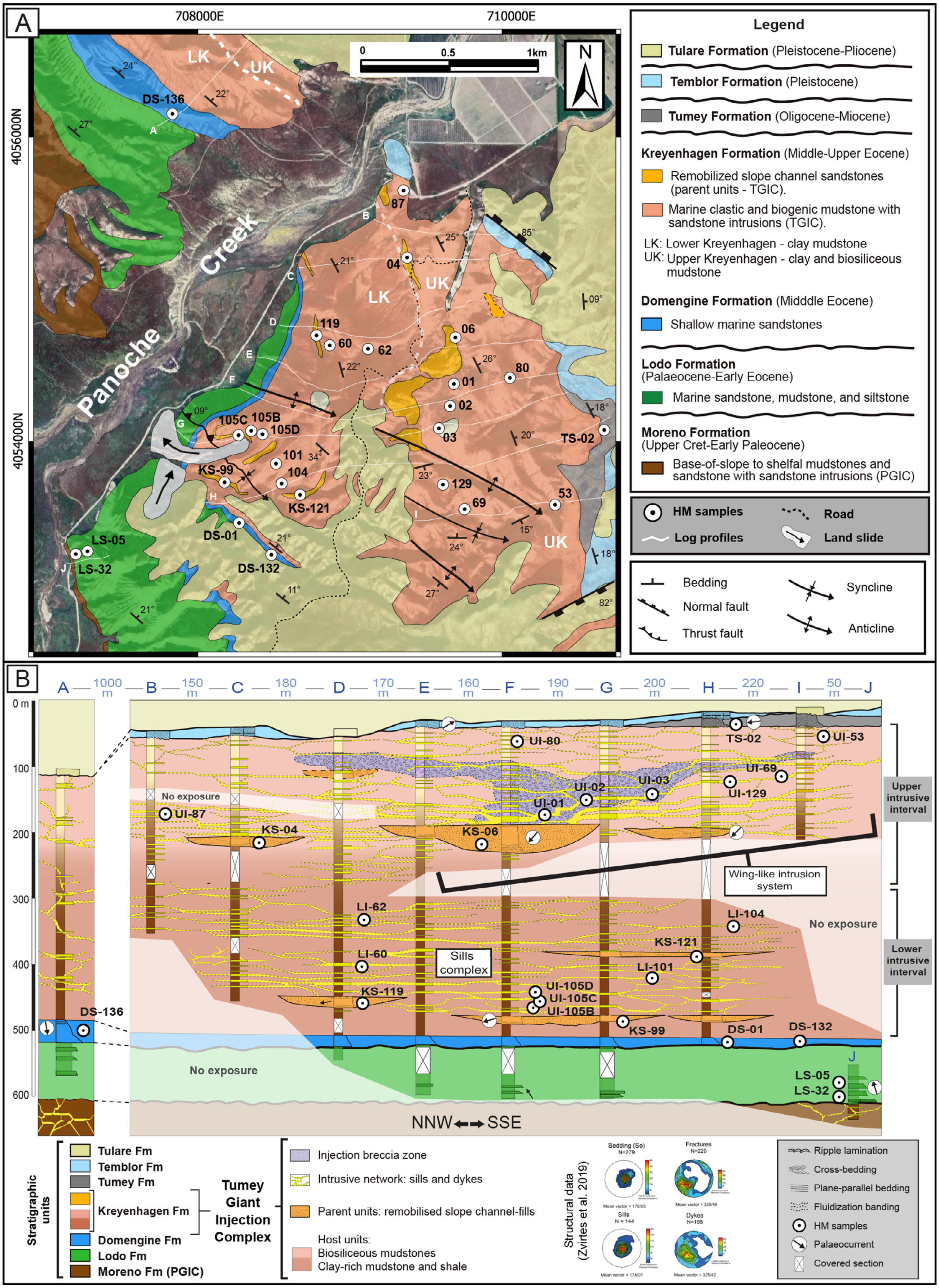

FIGURE 4 | (A) Geological map of Tumey Hill area with location of analysed samples. (B) Log correlation panel and samples location. Modified from Zvirtes et al. (2019).

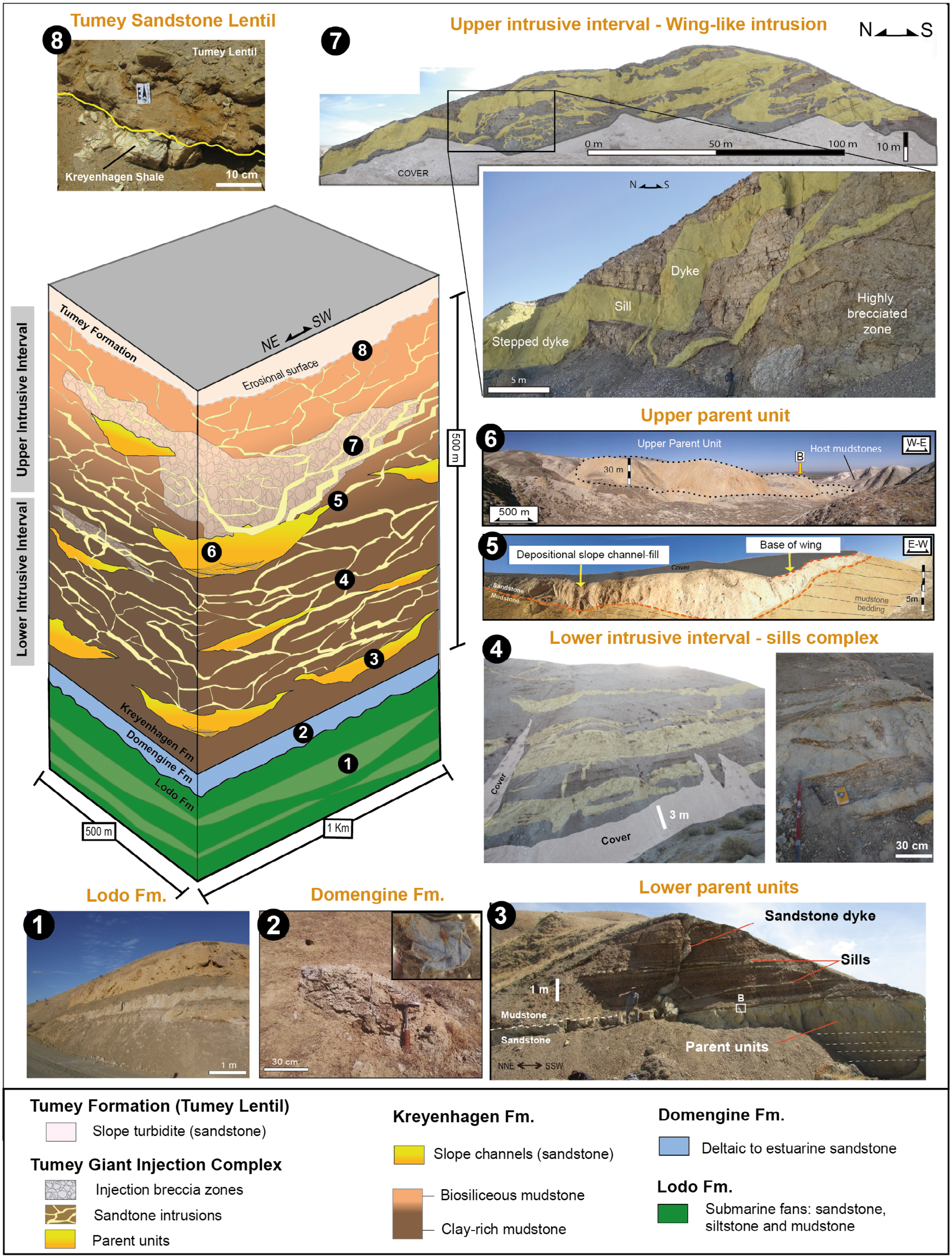

FIGURE 5 | Architecture and lithostratigraphy of the TGIC at Tumey Hills with representative outcrops (numbers 1–8).

TABLE 1 | Percentage of heavy mineral for individual samples (top number in each cell) and respective 90% confidence intervals (CIs) represented by numbers in brackets (low and high CIs) using Wilson Score Interval (Wilson 1927).

Sample	Unit	Al	An	Ap	At	Br	Ca	Cp	Cr	Ct	Ep	Gh	Gt	Ky	Lw	Mo	Op	Pm	Ru	Sa	Sl	Sp	St	To	Xe	Zr
UI-53B	UII	0.5 [0.1, 2.2]	2.0 [0.9, 4.4]	11.0 [7.9, 15.2]	0.0 [0.0, 1.3]	0.0 [0.0, 1.3]	1.5 [0.6, 3.7]	0.0 [0.0, 1.3]	0.0 [0.0, 1.3]	0.0 [0.0, 1.3]	41.0 [35.4, 46.8]	0.0 [0.0, 1.3]	12.5 [9.1, 16.9]	0.0 [0.0, 1.3]	0.0 [0.0, 1.3]	1.5 [0.6, 3.7]	0.0 [0.0, 1.3]	0.0 [0.0, 1.3]	1.0 [0.3, 3.0]	0.0 [0.0, 1.3]	0.0 [0.0, 1.3]	15.0 [11.3, 19.6]	0.0 [0.0, 1.3]	0.5 [0.1, 2.2]	0.0 [0.0, 1.3]	13.5 [10.0, 18.0]
UI-87A	UII	0.0 [0.0, 1.3]	2.5 [1.2, 5.0]	0.0 [0.0, 1.3]	0.5 [0.1, 2.2]	0.0 [0.0, 1.3]	0.5 [0.1, 2.2]	0.5 [0.1, 2.2]	0.0 [0.0, 1.3]	0.5 [0.1, 2.2]	64.0 [58.3, 69.4]	0.0 [0.0, 1.3]	3.5 [1.9, 6.3]	0.0 [0.0, 1.3]	0.0 [0.0, 1.3]	0.5 [0.1, 2.2]	0.5 [0.1, 2.2]	0.5 [0.1, 2.2]	1.5 [0.6, 3.7]	0.5 [0.1, 2.2]	0.0 [0.0, 1.3]	11.5 [8.3, 15.7]	3.5 [1.9, 6.3]	1.5 [0.6, 3.7]	0.0 [0.0, 1.3]	8.0 [5.4, 11.7]
UI-80B	UII	0.5 [0.1, 2.2]	0.5 [0.1, 2.2]	4.0 [2.3, 7.0]	0.0 [0.0, 1.3]	0.0 [0.0, 1.3]	0.0 [0.0, 1.3]	0.0 [0.0, 1.3]	0.0 [0.0, 1.3]	0.0 [0.0, 1.3]	74.5 [69.1, 79.2]	0.0 [0.0, 1.3]	4.5 [2.6, 7.6]	0.0 [0.0, 1.3]	0.5 [0.1, 2.2]	0.0 [0.0, 1.3]	0.0 [0.0, 1.3]	0.5 [0.1, 2.2]	0.5 [0.1, 2.2]	0.5 [0.1, 2.2]	0.0 [0.0, 1.3]	8.5 [5.8, 12.3]	0.5 [0.1, 2.2]	2.5 [1.2, 5.0]	0.0 [0.0, 1.3]	2.5 [1.2, 5.0]
UI-69B	UII	0.0 [0.0, 1.3]	1.5 [0.6, 3.7]	0.0 [0.0, 1.3]	0.5 [0.1, 2.2]	0.0 [0.0, 1.3]	1.5 [0.6, 3.7]	0.0 [0.0, 1.3]	0.0 [0.0, 1.3]	0.0 [0.0, 1.3]	63.0 [57.2, 68.4]	0.0 [0.0, 1.3]	5.5 [3.4, 8.8]	0.0 [0.0, 1.3]	0.0 [0.0, 1.3]	0.0 [0.0, 1.3]	0.0 [0.0, 1.3]	0.0 [0.0, 1.3]	2.0 [0.9, 4.4]	0.5 [0.1, 2.2]	0.0 [0.0, 1.3]	10.5 [7.4, 14.6]	0.5 [0.1, 2.2]	2.0 [0.9, 4.4]	0.0 [0.0, 1.3]	12.5 [9.1, 16.9]
UI-129B	UII	0.0 [0.0, 1.3]	6.5 [4.2, 10.0]	1.0 [0.3, 3.0]	1.5 [0.6, 3.7]	0.0 [0.0, 1.3]	0.0 [0.0, 1.3]	1.0 [0.3, 3.0]	0.0 [0.0, 1.3]	0.0 [0.0, 1.3]	1.5 [0.6, 3.7]	0.0 [0.0, 1.3]	10.0 [7.0, 14.0]	4.5 [2.6, 7.6]	0.0 [0.0, 1.3]	2.0 [0.9, 4.4]	0.5 [0.1, 2.2]	0.0 [0.0, 1.3]	5.5 [3.4, 8.8]	1.0 [0.3, 3.0]	0.0 [0.0, 1.3]	1.0 [0.3, 3.0]	4.5 [2.6, 7.6]	7.0 [4.6, 10.6]	0.5 [0.1, 2.2]	52.0 [46.2, 57.7]
UI-03	UII	0.0 [0.0, 1.3]	8.0 [5.4, 11.7]	0.0 [0.0, 1.3]	0.5 [0.1, 2.2]	0.5 [0.1, 2.2]	0.0 [0.0, 1.3]	0.0 [0.0, 1.3]	0.0 [0.0, 1.3]	0.0 [0.0, 1.3]	1.0 [0.3, 3.0]	0.0 [0.0, 1.3]	2.5 [1.2, 5.0]	2.0 [0.9, 4.4]	0.0 [0.0, 1.3]	2.0 [0.9, 4.4]	0.0 [0.0, 1.3]	0.0 [0.0, 1.3]	6.0 [3.8, 9.4]	1.0 [0.3, 3.0]	0.0 [0.0, 1.3]	5.0 [3.0, 8.2]	4.0 [2.3, 7.0]	9.5 [6.6, 13.5]	0.5 [0.1, 2.2]	57.5 [51.7, 63.1]
UI-02	UII	0.5 [0.1, 2.2]	1.5 [0.6, 3.7]	1.0 [0.3, 3.0]	0.0 [0.0, 1.3]	0.0 [0.0, 1.3]	6.5 [4.2, 10.0]	0.0 [0.0, 1.3]	0.0 [0.0, 1.3]	0.5 [0.1, 2.2]	53.0 [47.2, 58.7]	0.0 [0.0, 1.3]	8.0 [5.4, 11.7]	1.0 [0.3, 3.0]	0.0 [0.0, 1.3]	0.5 [0.1, 2.2]	0.0 [0.0, 1.3]	0.5 [0.1, 2.2]	0.5 [0.1, 2.2]	0.5 [0.1, 2.2]	0.0 [0.0, 1.3]	15.5 [11.8, 20.2]	0.5 [0.1, 2.2]	2.0 [0.9, 4.4]	0.0 [0.0, 1.3]	8.0 [5.4, 11.7]
UI-01	UII	0.5 [0.1, 2.2]	0.5 [0.1, 2.2]	2.5 [1.2, 5.0]	0.0 [0.0, 1.3]	0.0 [0.0, 1.3]	3.5 [1.9, 6.3]	0.0 [0.0, 1.3]	0.0 [0.0, 1.3]	0.0 [0.0, 1.3]	64.5 [58.8, 69.8]	0.0 [0.0, 1.3]	6.5 [4.2, 10.0]	0.5 [0.1, 2.2]	1.0 [0.3, 3.0]	0.0 [0.0, 1.3]	0.0 [0.0, 1.3]	0.0 [0.0, 1.3]	1.0 [0.3, 3.0]	0.0 [0.0, 1.3]	0.0 [0.0, 1.3]	10.5 [7.4, 14.6]	0.0 [0.0, 1.3]	1.0 [0.3, 3.0]	0.0 [0.0, 1.3]	8.0 [5.4, 11.7]
UI-06	UPU	0.0 [0.0, 1.3]	0.0 [0.0, 1.3]	1.0 [0.3, 3.0]	0.0 [0.0, 1.3]	0.0 [0.0, 1.3]	0.0 [0.0, 1.3]	0.0 [0.0, 1.3]	0.0 [0.0, 1.3]	0.0 [0.0, 1.3]	43.0 [37.4, 48.8]	0.0 [0.0, 1.3]	15.0 [11.3, 19.6]	0.0 [0.0, 1.3]	0.0 [0.0, 1.3]	0.0 [0.0, 1.3]	0.0 [0.0, 1.3]	0.0 [0.0, 1.3]	2.5 [1.2, 5.0]	0.0 [0.0, 1.3]	0.0 [0.0, 1.3]	18.5 [14.4, 23.4]	0.0 [0.0, 1.3]	0.0 [0.0, 1.3]	0.0 [0.0, 1.3]	20.0 [15.8, 25.0]
UI-04	UPU	1.5 [0.6, 3.7]	3.5 [1.9, 6.3]	6.5 [4.2, 10.0]	0.0 [0.0, 1.3]	0.0 [0.0, 1.3]	0.0 [0.0, 1.3]	0.5 [0.1, 2.2]	0.0 [0.0, 1.3]	0.0 [0.0, 1.3]	45.0 [39.3, 50.8]	0.0 [0.0, 1.3]	10.0 [7.0, 14.0]	0.0 [0.0, 1.3]	1.0 [0.3, 3.0]	1.5 [0.6, 3.7]	0.0 [0.0, 1.3]	0.0 [0.0, 1.3]	0.5 [0.1, 2.2]	0.5 [0.1, 2.2]	0.0 [0.0, 1.3]	18.0 [14.0, 22.9]	1.5 [0.6, 3.7]	2.0 [0.9, 4.4]	0.0 [0.0, 1.3]	8.0 [5.4, 11.7]
UI-62	LII	0.5 [0.1, 2.2]	2.0 [0.9, 4.4]	0.5 [0.1, 2.2]	0.5 [0.1, 2.2]	0.0 [0.0, 1.3]	0.0 [0.0, 1.3]	0.0 [0.0, 1.3]	0.0 [0.0, 1.3]	0.5 [0.1, 2.2]	9.0 [6.2, 12.9]	0.0 [0.0, 1.3]	16.5 [12.6, 21.3]	2.5 [1.2, 5.0]	0.0 [0.0, 1.3]	0.5 [0.1, 2.2]	0.5 [0.1, 2.2]	0.0 [0.0, 1.3]	3.0 [1.6, 5.7]	1.0 [0.3, 3.0]	0.0 [0.0, 1.3]	29.0 [24.0, 34.5]	2.0 [0.9, 4.4]	1.5 [0.6, 3.7]	0.0 [0.0, 1.3]	30.5 [25.4, 36.1]
UI-104	LII	2.0 [0.9, 4.4]	4.5 [2.6, 7.6]	8.0 [5.4, 11.7]	0.5 [0.1, 2.2]	0.0 [0.0, 1.3]	0.0 [0.0, 1.3]	0.0 [0.0, 1.3]	0.5 [0.1, 2.2]	0.0 [0.0, 1.3]	3.0 [1.6, 5.7]	0.0 [0.0, 1.3]	15.0 [11.3, 19.6]	1.0 [0.3, 3.0]	0.0 [0.0, 1.3]	0.0 [0.0, 1.3]	0.0 [0.0, 1.3]	0.0 [0.0, 1.3]	1.5 [0.6, 3.7]	0.0 [0.0, 1.3]	0.0 [0.0, 1.3]	43.5 [37.9, 49.3]	2.0 [0.9, 4.4]	7.0 [4.6, 10.6]	0.0 [0.0, 1.3]	11.5 [8.3, 15.7]

(Continues)

TABLE 1 | (Continued)

Sample	Unit	Al	An	Ap	At	Br	Ca	Cp	Cr	Ct	Ep	Gh	Gt	Ky	Lw	Mo	Op	Pm	Ru	Sa	Sl	Sp	St	To	Xe	Zr
UI-101	LII	0.5 [0.1, 2.2]	2.5 [1.2, 5.0]	11.0 [7.9, 15.2]	0.5 [0.1, 2.2]	0.0 [0.0, 1.3]	0.0 [0.0, 1.3]	0.0 [0.0, 1.3]	0.0 [0.0, 1.3]	0.0 [0.0, 1.3]	44.5 [38.8, 50.3]	0.0 [0.0, 1.3]	6.5 [4.2, 10.0]	0.0 [0.0, 1.3]	0.0 [0.0, 1.3]	0.0 [0.0, 1.3]	0.0 [0.0, 1.3]	0.0 [0.0, 1.3]	0.5 [0.1, 2.2]	0.5 [0.1, 2.2]	0.0 [0.0, 1.3]	25.5 [20.8, 30.9]	0.0 [0.0, 1.3]	2.0 [0.9, 4.4]	0.0 [0.0, 1.3]	6.0 [3.8, 9.4]
UI-105D	LII	1.5 [0.6, 3.7]	3.5 [1.9, 6.3]	11.5 [8.3, 15.7]	1.5 [0.6, 3.7]	0.0 [0.0, 1.3]	0.0 [0.0, 1.3]	0.0 [0.0, 1.3]	1.5 [0.6, 3.7]	0.0 [0.0, 1.3]	7.5 [5.0, 11.2]	0.0 [0.0, 1.3]	15.5 [11.8, 20.2]	0.5 [0.1, 2.2]	0.5 [0.1, 2.2]	0.5 [0.1, 2.2]	0.0 [0.0, 1.3]	2.0 [0.9, 4.4]	1.0 [0.3, 3.0]	2.0 [0.9, 4.4]	0.0 [0.0, 1.3]	27.0 [22.2, 32.4]	1.0 [0.3, 3.0]	3.0 [1.6, 5.7]	0.0 [0.0, 1.3]	20.0 [15.8, 25.0]
UI-105C	LII	0.5 [0.1, 2.2]	5.0 [3.0, 8.2]	4.0 [2.3, 7.0]	1.0 [0.3, 3.0]	0.0 [0.0, 1.3]	1.0 [0.3, 3.0]	0.0 [0.0, 1.3]	0.5 [0.1, 2.2]	0.0 [0.0, 1.3]	17.0 [13.1, 21.8]	0.0 [0.0, 1.3]	17.0 [13.1, 21.8]	0.0 [0.0, 1.3]	3.5 [1.9, 6.3]	0.5 [0.1, 2.2]	0.0 [0.0, 1.3]	0.5 [0.1, 2.2]	1.0 [0.3, 3.0]	5.0 [3.0, 8.2]	0.0 [0.0, 1.3]	27.5 [22.6, 33.0]	1.0 [0.3, 3.0]	2.0 [0.9, 4.4]	0.0 [0.0, 1.3]	13.0 [9.6, 17.4]
UI-105B	LII	1.0 [0.3, 3.0]	1.5 [0.6, 3.7]	15.0 [11.3, 19.6]	0.5 [0.1, 2.2]	0.0 [0.0, 1.3]	0.0 [0.0, 1.3]	0.0 [0.0, 1.3]	1.5 [0.6, 3.7]	0.0 [0.0, 1.3]	15.5 [11.8, 20.2]	0.0 [0.0, 1.3]	15.0 [11.3, 19.6]	0.5 [0.1, 2.2]	0.0 [0.0, 1.3]	1.0 [0.3, 3.0]	0.0 [0.0, 1.3]	1.0 [0.3, 3.0]	1.0 [0.3, 3.0]	1.0 [0.3, 3.0]	0.0 [0.0, 1.3]	27.0 [22.2, 32.4]	1.0 [0.3, 3.0]	1.5 [0.6, 3.7]	0.0 [0.0, 1.3]	16.0 [12.2, 20.7]
UI-60	LII	0.5 [0.1, 2.2]	2.0 [0.9, 4.4]	15.5 [11.8, 20.2]	0.0 [0.0, 1.3]	0.0 [0.0, 1.3]	14.0 [10.4, 18.5]	7.5 [5.0, 11.2]	0.0 [0.0, 1.3]	0.0 [0.0, 1.3]	24.0 [19.4, 29.3]	0.0 [0.0, 1.3]	4.5 [2.6, 7.6]	0.5 [0.1, 2.2]	0.0 [0.0, 1.3]	0.5 [0.1, 2.2]	3.5 [1.9, 6.3]	0.0 [0.0, 1.3]	1.5 [0.6, 3.7]	0.0 [0.0, 1.3]	0.0 [0.0, 1.3]	16.0 [12.2, 20.7]	1.5 [0.6, 3.7]	1.5 [0.6, 3.7]	0.0 [0.0, 1.3]	7.0 [4.6, 10.6]
KS-121	LPU	3.0 [1.6, 5.7]	2.0 [0.9, 4.4]	20.5 [16.2, 25.6]	0.0 [0.0, 1.3]	0.0 [0.0, 1.3]	0.0 [0.0, 1.3]	0.0 [0.0, 1.3]	0.0 [0.0, 1.3]	0.5 [0.1, 2.2]	12.0 [8.7, 16.3]	0.0 [0.0, 1.3]	14.5 [10.9, 19.1]	1.5 [0.6, 3.7]	0.0 [0.0, 1.3]	1.0 [0.3, 3.0]	0.0 [0.0, 1.3]	0.0 [0.0, 1.3]	0.5 [0.1, 2.2]	1.0 [0.3, 3.0]	0.0 [0.0, 1.3]	27.0 [22.2, 32.4]	2.0 [0.9, 4.4]	3.0 [1.6, 5.7]	0.0 [0.0, 1.3]	11.5 [8.3, 15.7]
KS-119	LPU	1.0 [0.3, 3.0]	1.0 [0.3, 3.0]	13.5 [10.0, 18.0]	0.5 [0.1, 2.2]	0.0 [0.0, 1.3]	0.0 [0.0, 1.3]	0.0 [0.0, 1.3]	0.0 [0.0, 1.3]	0.0 [0.0, 1.3]	16.5 [12.6, 21.3]	0.0 [0.0, 1.3]	12.0 [8.7, 16.3]	0.0 [0.0, 1.3]	0.0 [0.0, 1.3]	0.0 [0.0, 1.3]	0.0 [0.0, 1.3]	0.0 [0.0, 1.3]	2.0 [0.9, 4.4]	2.0 [0.9, 4.4]	0.0 [0.0, 1.3]	33.0 [27.8, 38.7]	2.5 [1.2, 5.0]	3.5 [1.9, 6.3]	0.0 [0.0, 1.3]	12.5 [9.1, 16.9]
KS-99	LPU	0.0 [0.0, 1.3]	1.0 [0.3, 3.0]	5.0 [3.0, 8.2]	0.0 [0.0, 1.3]	0.0 [0.0, 1.3]	0.0 [0.0, 1.3]	0.0 [0.0, 1.3]	0.5 [0.1, 2.2]	0.0 [0.0, 1.3]	18.0 [14.0, 22.9]	0.0 [0.0, 1.3]	16.0 [12.2, 20.7]	1.5 [0.6, 3.7]	0.0 [0.0, 1.3]	1.0 [0.3, 3.0]	0.0 [0.0, 1.3]	0.0 [0.0, 1.3]	2.0 [0.9, 4.4]	1.5 [0.6, 3.7]	0.0 [0.0, 1.3]	25.0 [20.3, 30.3]	1.5 [0.6, 3.7]	1.5 [0.6, 3.7]	0.0 [0.0, 1.3]	25.5 [20.8, 30.9]
128A	DOM	0.5 [0.1, 2.2]	0.0 [0.0, 1.3]	4.5 [2.6, 7.6]	0.0 [0.0, 1.3]	0.0 [0.0, 1.3]	7.5 [5.0, 11.2]	2.5 [1.2, 5.0]	0.0 [0.0, 1.3]	0.0 [0.0, 1.3]	28.0 [23.1, 33.5]	0.0 [0.0, 1.3]	12.5 [9.1, 16.9]	0.0 [0.0, 1.3]	8.0 [5.4, 11.7]	0.0 [0.0, 1.3]	0.0 [0.0, 1.3]	2.0 [0.9, 4.4]	0.5 [0.1, 2.2]	17.0 [13.1, 21.8]	0.0 [0.0, 1.3]	13.5 [10.0, 18.0]	0.0 [0.0, 1.3]	1.5 [0.6, 3.7]	0.0 [0.0, 1.3]	2.0 [0.9, 4.4]
132-B	DOM	0.0 [0.0, 1.3]	0.0 [0.0, 1.3]	1.5 [0.6, 3.7]	0.0 [0.0, 1.3]	0.0 [0.0, 1.3]	9.5 [6.6, 13.5]	16.0 [12.2, 20.7]	0.0 [0.0, 1.3]	0.0 [0.0, 1.3]	11.5 [8.3, 15.7]	0.0 [0.0, 1.3]	4.5 [2.6, 7.6]	0.0 [0.0, 1.3]	10.5 [7.4, 14.6]	0.0 [0.0, 1.3]	11.5 [8.3, 15.7]	1.5 [0.6, 3.7]	0.5 [0.1, 2.2]	8.0 [5.4, 11.7]	0.0 [0.0, 1.3]	16.0 [12.2, 20.7]	0.0 [0.0, 1.3]	1.0 [0.3, 3.0]	0.0 [0.0, 1.3]	8.0 [5.4, 11.7]
136-C	DOM	0.0 [0.0, 1.3]	2.0 [0.9, 4.4]	6.0 [3.8, 9.4]	1.0 [0.3, 3.0]	0.0 [0.0, 1.3]	0.0 [0.0, 1.3]	0.0 [0.0, 1.3]	0.0 [0.0, 1.3]	0.0 [0.0, 1.3]	2.5 [1.2, 5.0]	0.0 [0.0, 1.3]	10.5 [7.4, 14.6]	0.0 [0.0, 1.3]	4.5 [2.6, 7.6]	0.0 [0.0, 1.3]	0.0 [0.0, 1.3]	0.0 [0.0, 1.3]	1.0 [0.3, 3.0]	3.0 [1.6, 5.7]	0.0 [0.0, 1.3]	45.0 [39.3, 50.8]	2.0 [0.9, 4.4]	7.5 [5.0, 11.2]	0.0 [0.0, 1.3]	15.0 [11.3, 19.6]
HM-05	LODO	0.0 [0.0, 1.3]	1.0 [0.3, 3.0]	0.0 [0.0, 1.3]	2.5 [1.2, 5.0]	0.0 [0.0, 1.3]	0.0 [0.0, 1.3]	0.0 [0.0, 1.3]	0.0 [0.0, 1.3]	0.0 [0.0, 1.3]	11.5 [8.3, 15.7]	0.0 [0.0, 1.3]	12.0 [8.7, 16.3]	0.0 [0.0, 1.3]	0.0 [0.0, 1.3]	0.5 [0.1, 2.2]	0.0 [0.0, 1.3]	0.0 [0.0, 1.3]	6.0 [3.8, 9.4]	0.5 [0.1, 2.2]	0.0 [0.0, 1.3]	1.0 [0.3, 3.0]	1.5 [0.6, 3.7]	17.0 [13.1, 21.8]	0.0 [0.0, 1.3]	46.5 [40.8, 52.3]
32-B	LODO	0.5 [0.1, 2.2]	0.0 [0.0, 1.3]	1.5 [0.6, 3.7]	1.0 [0.3, 3.0]	0.0 [0.0, 1.3]	0.5 [0.1, 2.2]	0.0 [0.0, 1.3]	0.0 [0.0, 1.3]	0.0 [0.0, 1.3]	24.0 [19.4, 29.3]	0.0 [0.0, 1.3]	11.5 [8.3, 15.7]	0.0 [0.0, 1.3]	0.0 [0.0, 1.3]	0.0 [0.0, 1.3]	0.0 [0.0, 1.3]	0.0 [0.0, 1.3]	0.5 [0.1, 2.2]	0.5 [0.1, 2.2]	0.0 [0.0, 1.3]	48.5 [42.7, 54.3]	0.5 [0.1, 2.2]	1.5 [0.6, 3.7]	0.0 [0.0, 1.3]	9.5 [6.6, 13.5]

Abbreviations: Al = allanite; An = andalusite; At = anatase; Ap = apatite; Br = brookite; Ca = calcic amphibole; Cp = clinopyroxene; Cr = chrome spinel; Ct = chloritoid; Ep = epidote; Gh = gahnite; Gt = garnet; Ky = kyanite; Lws = lawsonite; Mo = monazite; Op = orthopyroxene; Pm = pumpellyite; Rt = rutile; Sa = sodic amphibole (glaucophane); Sp = titanite; St = staurolite; To = tourmaline; Xe = xenotime; Zr = Zircon.

Formula: → $ABi = \frac{A}{A+B} \times 100$. The letters A and B represent the two different minerals chosen for analysis.

Provenance indices were based on the proportion of two minerals with similar densities and hydraulic behaviours to minimize the effects of hydraulic sorting and diagenetic dissolution, providing information of original source rock characteristics (A. C. Morton 1985; Morton and Hallsworth 1994).

- *MZi* (Monazite-Zircon Index) tracks the relationship between monazite and zircon, which are both dense and stable minerals. Monazite is typically derived from granites and high-grade metamorphic rocks (metasediments), whereas zircon is ubiquitous in many crustal rocks.
- *GZi* (Garnet-Zircon Index) contrasts garnet with zircon and it is used to identify metamorphic inputs.
- *CZi* (Chrome Spinel-Zircon Index) compares chrome spinel (chromite) to zircon as a diagnostic tool for identifying ultramafic or mafic sources.
- *RuZi* (Rutile-Zircon Index) compares minerals that are ultra-stable. Rutile is often associated with high-grade and high-pressure metamorphic rocks.
- *ATi* (Apatite-Tourmaline Index) compares apatite (less stable) to tourmaline (extremely stable).

Additionally, the proportion of blueschist minerals (expressed as % of whole assemblage) to track any inputs from emergent ophiolitic complexes, and the proportion of minerals associated with low- and medium-grade metasedimentary successions were assessed.

To analyse hydraulic effects during sand injection, *ZTi* (Zircon-Tourmaline Index) was calculated. *ZTi* is a density-sensitive parameter where both minerals are ultra-stables but with contrasting densities (high-density zircon and low-density tourmaline). This parameter is expected to express changes throughout the complex, assuming variations in pressure gradients and fluid flow conditions during sand emplacement.

For sediment maturity, mechanical stability and weathering effects, ZTR index was calculated based on the sum of three ultra-stable minerals (zircon, tourmaline and rutile) over the total heavy mineral translucent grains (Hubert 1962).

$$\text{Formula: } \rightarrow \text{ZTR} = \frac{\text{Zircon} + \text{Tourmaline} + \text{Rutile}}{\text{Total heavy mineral translucent grains}} \times 100$$

For depositional units, high ZTR values indicate mature assemblages that can suggest terrestrial weathering and recycling along the sediment routing from source-to-sink, whereas low ZTR values are typical of immature sediments from first-cycle inputs. Due to the high resistance to mechanical abrasion and weathering, these minerals should also resist sand injection processes and post-injection diagenetic and surface weathering.

3.2 | Statistical Analysis of Heavy Minerals

To ensure dataset validity, uncertainties were characterized at two distinct scales to distinguish between analytical precision and geological heterogeneity. The dataset used for the statistical analysis is provided in the Appendix A.

3.2.1 | Single Sample Uncertainty

For individual samples, 90% confidence intervals (CIs) were calculated using the Wilson Score Interval (Wilson 1927) (Table 1). Unlike the Gaussian approximation (assumption of normal distribution) traditionally used in geological provenance studies (e.g., Van der Plas and Tobi 1965), the Wilson interval provides robust asymmetric error estimates. This is critical for heavy mineral data with small grain counts ($n < 50$) or proportions near the 0% or 100% boundaries, as it accurately reflects the counting statistics inherent to restricted counts and avoids physically impossible negative confidence intervals (Brown et al. 2001). This was performed both on full assemblage count data and calculated parameters.

3.2.2 | Group/Unit-Level Characterization

To characterize the composition of the architectural elements, we implemented a Bayesian Hierarchical Beta-Binomial model (Gelman et al. 2013). While traditional pooling (summing grains across all samples from the same unit) assumes that samples are drawn from a homogeneous population, geological units typically exhibit overdispersion (compositional variation between samples that exceeds analytical counting error) (Weltje 2002).

The hierarchical model accounts for this by modelling the unit proportion as a Beta distribution rather than a fixed value. This approach facilitates 'partial pooling', where group estimates are weighted by sample size while propagating the uncertainty caused by natural sedimentological heterogeneity (McElreath 2020; Vermeesch 2018). The resulting 90% Highest Density Intervals (HDIs) represent the most probable compositional range for the geological unit itself, rather than for any single sample drawn from it. This modelling was applied in two stages:

1. Bulk Assemblage: The model was applied to the full grain counts to generate robust centroids for the major mineral phases.
2. Varietal Indices: Each provenance index (e.g., *ATi*, *GZi*) was modelled as an independent Beta-Binomial system. This treats each index as a distinct mineralogical subsystem (e.g., Garnet vs. Zircon), ensuring that the resulting Group Centroid (Median Posterior Probability) for that index is mathematically independent of the other indices

3.2.3 | Quantitative Provenance Analysis

To objectively compare the architectural elements, we employed two complementary multivariate techniques adapted for compositional data.

3.2.3.1 | Principal Component Analysis (PCA). To identify the primary mineralogical gradients driving the variation, Principal Component Analysis was performed at two scales:

1. Sample-Level PCA: First, the analysis was applied to the entire dataset of individual samples. This allowed for the assessment of total dataset variance and intra-unit heterogeneity (overdispersion) prior to grouping.
2. Centroid-Level PCA: Second, PCA was performed on the robust Bayesian Group Centroids. This step distills the primary provenance vectors, removing the noise of individual sample outliers to clearly define the fundamental relationships between architectural elements (Davis 2002).

Because the data are compositional (constrained to 100%), standard PCA is mathematically invalid on raw percentages. We therefore applied the Centered Log-Ratio (clr) transformation prior to both analyses (Aitchison 1983). This transformation maps the closed compositional data into real Euclidean space, ensuring that the resulting Principal Components accurately reflect the variation in the underlying mineral populations (Weltje 2002). Prior to transformation, zero values (common in trace phases) were managed using a multiplicative replacement strategy, substituting zeros with a small constant ($\delta = 0.01$) to permit log-ratio transformation (Martín-Fernández et al. 2003).

3.2.3.2 | Hierarchical Clustering (Provenance Tree). To quantify the total compositional similarity between units, we constructed a hierarchical dendrogram based on the Aitchison Distance (Aitchison 1986). Distances were calculated as the Euclidean distance between the clr-transformed group centroids. The Aitchison distance is preferred over standard Euclidean metrics because it is scale-invariant and respects the relative magnitude of components rather than their absolute values (Chayes 1960; Pearson 1897). The ‘Provenance Family Tree’ was then constructed from this distance matrix using Ward's Minimum Variance Method (Ward 1963). Ward's method was selected because it minimizes the total within-cluster variance, producing compact, spherical clusters that objectively group geological units based on their total mineralogical affinity (Vermeesch et al. 2016).

3.2.4 | Provenance Index Analysis (Standardized Data)

To isolate specific provenance signals independent of hydraulic sorting and burial diagenesis, we analysed the suite of varietal indices (e.g., *ATi*, *GZi*, *RuZi*). Because these indices are independent variables with vastly different numerical ranges (e.g., *ATi* 0–100 vs. *RuZi* 0–15), raw distance calculations would be biased toward indices with larger magnitudes.

3.2.4.1 | PCA and Clustering of Indices. To resolve this, the independent Bayesian centroids for the selected indices were first standardized to Z-scores, ensuring each index contributed equally to the analysis (Davis 2002). PCA was performed on these standardized variables to identify the primary vectors of source lithology and durability. Similarly, a separate hierarchical dendrogram was constructed using the Standardized Euclidean Distance and Ward's method, grouping units based specifically on their shared index characteristics.

3.2.4.2 | Qualitative Index Analysis. Complementary to the multivariate statistical approach, bivariate cross plots of provenance-sensitive heavy mineral indices were constructed for qualitative assessment. While standard ultrastable indices (e.g., *ATi*, *GZi*) showed considerable overlap between units, specific discrimination was achieved by plotting the abundance of diagnostic high-pressure/low-temperature (*HP/LT*) metamorphic phases. Cross plots incorporating the total percentage of blueschist-facies minerals (Lawsonite + Sodic Amphibole) were utilized to specifically isolate inputs from emergent ophiolitic complexes.

3.2.5 | Assemblage Diversity and Maturity

To quantify the mineralogical maturity of the samples, we calculated the Shannon Entropy (H) for each assemblage (Shannon 1948). In sedimentary petrology, entropy serves as a robust proxy for sorting and weathering intensity. High entropy values indicate a diverse, immature suite derived from mixed sources, while low entropy values characterize compositionally mature assemblages dominated by a few ultrastable phases, reflecting extensive recycling or aggressive diagenetic filtering (Pelto 1954).

4 | Results

4.1 | Heavy Mineral Assemblages

Analysis of 26 samples revealed a diverse assemblage of 24 mineral species (Figure 6; Table 1) reflecting the high degree of heterogeneity of clastic material deposited in the San Joaquin basin. Median percentages of groups were calculated with confidence intervals of 90% (Table 1); mineral units were categorized by abundance thresholds into three groups: major (≥ 8%), subordinate (1%–8%) and rare (< 1%).

Lodo Formation present five major minerals: zircon (*Mdn* = 28.1%, 90% CI [11.2, 47.8]), titanite (*Mdn* = 23.5%, 90% CI [3.1, 46.6]), epidote (*Mdn* = 18.4%, 90% CI [9.7, 26.9]), garnet (*Mdn* = 12,4%, 90% CI [7.5, 18.6]) and tourmaline (*Mdn* = 10.4%, 90% CI [1.9, 23.1]). Rutile, anatase, staurolite, andalusite, apatite, sodic amphibole and monazite are subordinate, with rare calcic amphibole, chrome spinel and allanite.

Domengine Formation present the most diverse HM assemblages with six major minerals: titanite (*Mdn* = 25.6%, 90% CI [13.8, 37.6]), epidote (*Mdn* = 14.6%, 90% CI [5, 26.6]), sodic amphibole (*Mdn* = 9.8%, 90% CI [4.1, 17]), garnet (*Mdn* = 9.6%, 90% CI [6.1, 14.5]), zircon (*Mdn* = 8.9%, 90% CI [3.6, 16.6]), lawsonite (*Mdn* = 8.1%, 90% CI [4.8, 12.1]). Clinopyroxene, calcic amphibole, apatite, tourmaline, pumpellyite, andalusite, rutile, staurolite and anatase are subordinate, with rare allanite, chrome spinel, brookite and chloritoid.

The depositional sandstones of Kreyenhagen Formation present five major minerals: titanite (*Mdn* = 24.4%, 90% CI [19.9, 29]),

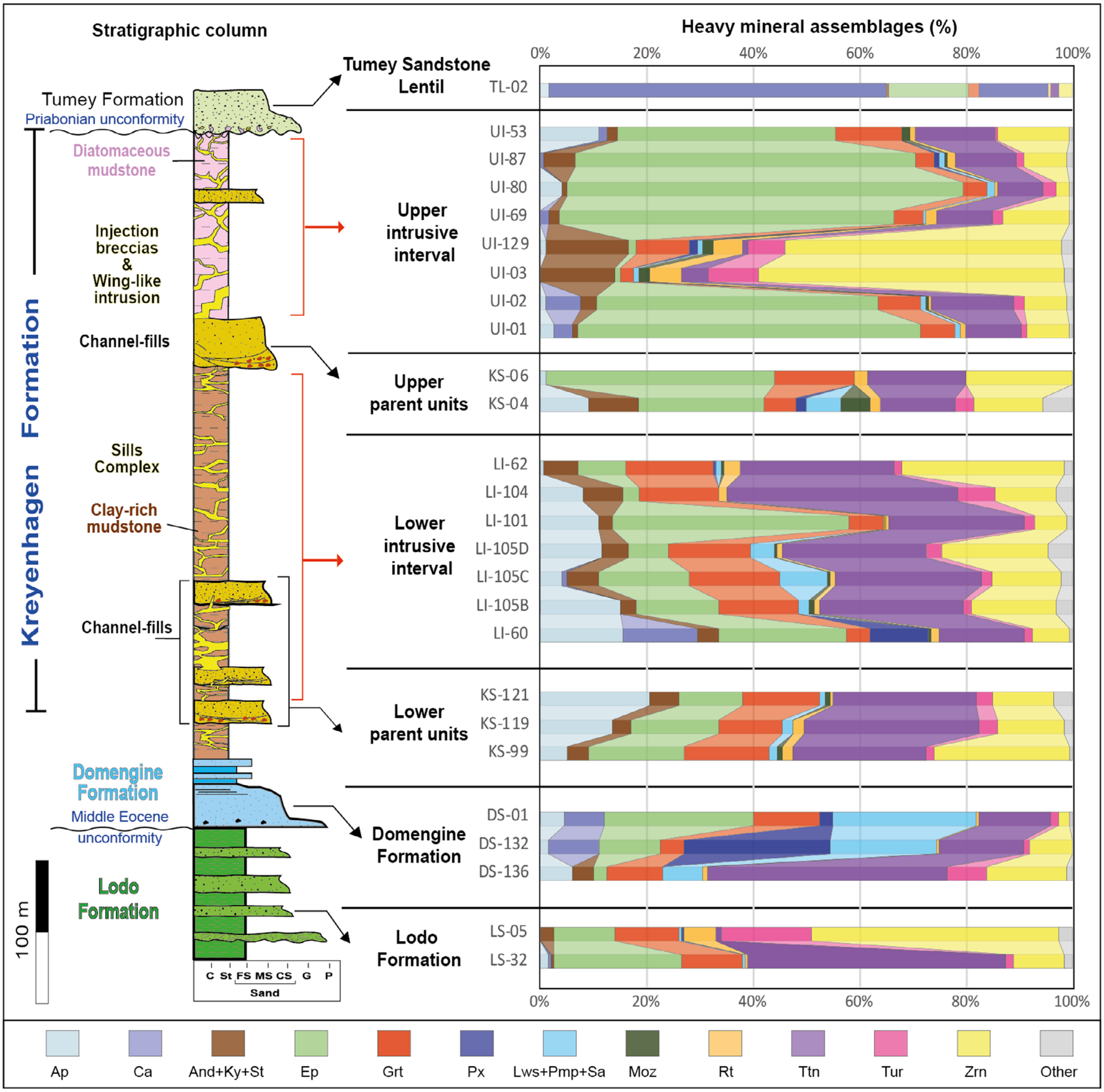

FIGURE 6 | Idealized lithostratigraphic column of study area (left) and proportions (%) of heavy mineral assemblage of samples represented in bar diagram (right). Ap, apatite; Ca, calcic amphibole; And, andalusite; Ky, kyanite; St, staurolite; Ep, epidote; Grt, garnet; Px, pyroxene; Lws, lawsonite; Pmp, pumpellyite; Sa, sodic amphibole; Moz, monazite; Rt, rutile; Tnt, titanite; Tur, tourmaline; Zrn, zircon.

zircon (*Mdn* = 15.8%, 90% CI [10.4, 21]), epidote (*Mdn* = 27.2%, 90% CI [17.4, 38.2]), garnet (*Mdn* = 13.8%, 90% CI [11.3, 16.8]) and apatite (*Mdn* = 9.5%, 90% CI [4.47, 15.8]). Tourmaline, sodic amphibole, monazite, staurolite, andalusite, rutile, allanite, and kyanite are subordinate with rare pyroxene, calcic amphibole, anatase and xenotime.

The sandstone intrusions present assemblages dominated by four major minerals: epidote (*Mdn* = 30.6%, 90% CI [20.6, 41.2]), zircon (*Mdn* = 18.5%, 90% CI [13, 24.7]), titanite (*Mdn* = 18.2%, 90% CI [13.5, 23.1]) and garnet (*Mdn* = 9.6%, 90% CI [7.4, 11.9]), with subordinate apatite, tourmaline, calcic amphibole, staurolite, rutile, sodic amphibole, monazite, pyroxene and kyanite and rare allanite, anatase, chrome spinel and xenotime.

4.2 | Mineral Assemblages Diversity and Compositional Similarities

4.2.1 | Compositional Trends (PCA)

Principal Component Analysis using centered log-ratio transformation illustrates the relative Aitchison distances between samples (Figure 7A). It is observed that the Kreyenhagen depositional sandstones concentrate in the upper section of the

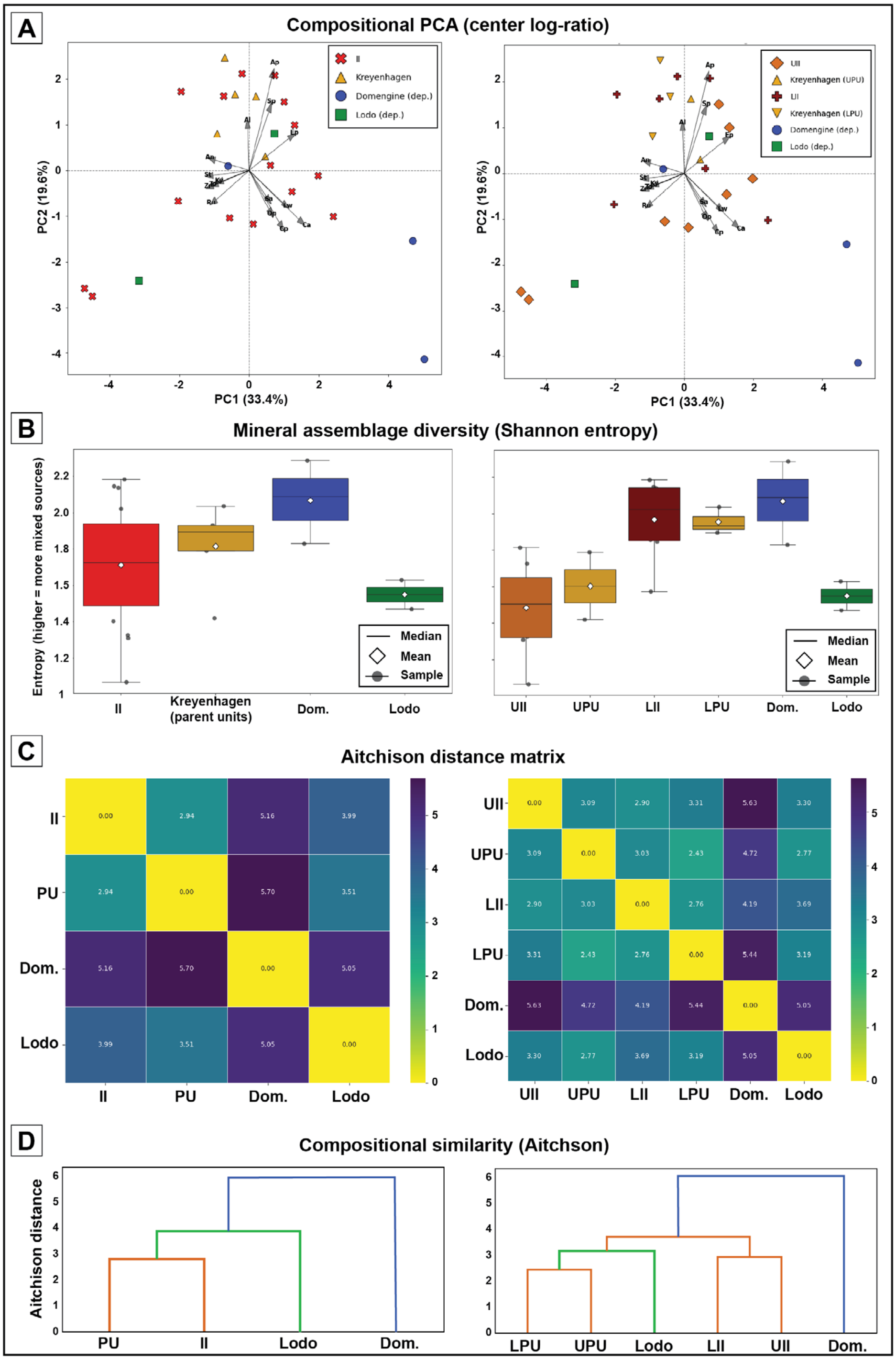

	II	PU	Dom.	Lodo
II	0.00	2.94	5.16	3.99
PU	2.94	0.00	5.70	3.51
Dom.	5.16	5.70	0.00	5.05
Lodo	3.99	3.51	5.05	0.00

	UII	UPU	LII	LPU	Dom.	Lodo
UII	0.00	3.09	2.90	3.31	5.63	3.30
UPU	3.09	0.00	3.03	2.43	4.72	2.77
LII	2.90	3.03	0.00	2.76	4.19	3.69
LPU	3.31	2.43	2.76	0.00	5.44	3.19
Dom.	5.63	4.72	4.19	5.44	0.00	5.05
Lodo	3.30	2.77	3.69	3.19	5.05	0.00

FIGURE 7 | Mineral Assemblages Diversity and Compositional Similarities analysis for depositional and intrusive sandstones (left side diagrams) and discrimination between lower and upper intrusive intervals (right side diagrams). (A) Composition PCA analysis based on centered log ratios. (B) Shannon entropy for different groups of samples. Values can be accessed in the appendix at Tables A2 and A3. (C) Aitchison Distance Matrix. Values in the appendix in Tables A4 and A5. (D) Dendrogram of Compositional Similarities between groups constructed using Ward's method and Aitchison distance. Values in the appendix in Tables A4 and A5. Note the good correlation between parent units and injectites.

diagram (Aitchson distances varying between 0.3 and 2.5 in the vertical axis and −1 and 2 in the horizontal axis) with affinities with apatite, allanite, titanite and epidote, which are relatively more immature assemblages. Intrusions from the LII are mostly following the same pattern, with the exception of two samples that present negative values in the vertical axis with affinities with more stable mineralogy (e.g., zircon, tourmaline, rutile). Samples from UII present greater scatter, with vertical distances ranging from positive (1–2) to highly negative (−3 and −4). Similar behaviour is observed in the Lodo sandstones. In contrast, two sandstones from the Domengine Formation display distinct signatures, with high positive horizontal values (>4) and negative vertical values. These signatures correlate strongly with pyroxenes and blueschist-facies minerals, specifically sodic amphibole (glaucophane) and lawsonite. One LII sample plots near this group, albeit closer to the centre.

4.2.2 | Mineralogical Diversity (Shannon Entropy)

A Shannon entropy diagram was constructed to quantify mineralogical diversity (Figure 7B), where higher entropy suggests a more varied detrital provenance.

Highest Diversity: Domengine Formation assemblages with entropy median of 2.1.

Moderate Diversity: Lower Parent Units (LPU) and Lower Intrusive Interval (LII) showed higher median values (1.9), indicating relative intermediate compositional variability.

Lowest Diversity: Lodo Formation, Upper Parent Units (UPU) and Upper Intrusive Interval (UII) recorded the lowest median entropy (1.4–1.5).

4.2.3 | Compositional Similarities

The Aitchison distance matrix (Figure 7C) reveals that the shortest distances, thus the highest compositional affinities, exist between the Kreyenhagen parent units (PU) and the Intrusive Intervals (II). Conversely, these units show significant dissimilarity when compared to the Lodo sandstones and even greater distances from the Domengine sandstones. This hierarchical relationship is further supported by the dendrogram analysis (Figure 7D). When comparing sub-units, the highest similarities are found within the Kreyenhagen channel-fill pairs and between the two intrusive intervals.

4.3 | Provenance-Sensitive Heavy Mineral Indices

Provence signatures from depositional and intrusive units were assessed by a proxy of mineral indices using *RuZi*, *MZi*, *CZi* and *ATi* (Figure 8A–D) and the percentage of metasedimentary and blueschist minerals cross plotted over *GZi* (Figure 8E,F). For better visualization and enhancement between units, the cross plots are based on PCA of index centroids with 90% HDI.

RuZi shows that all depositional units present similar ranges and overlapping values, suggesting high-grade metamorphic rocks supplying sediments into their specific sediment routes. The sandstone intrusions present slightly higher *RuZi* with overlaps with Lodo and Kreyenhagen sandstones.

The *MZi* indicates a strong affinity between sandstone intrusions and Kreyenhagen channel-fills, contrasting with lower values from Lodo and Domengine samples. Higher *MZi* indicates that the channels, and to a lesser extent Lodo fans, were sourced from granites and metamorphic rocks (metasediments), which are typical in the Sierra Nevada province to the east. On the other hand, the extremely lower values for Domengine indicate less contribution from these source types.

The *CZi* cross plot shows similar values among Kreyenhagen and Lodo sandstones and most of the intrusive intervals, with extremely low median values ranging from 1 to 2. The exceptions are dykes of LII and Domengine sandstones which present higher values of 6 and 3, respectively, suggesting ultramafic or mafic sources from erosion of oceanic crust or mantle-derived rocks.

ATi shows that Domengine, Kreyenhagen, and most of the intrusive sandstone present high values (60–85). In contrast, Lodo and the sills of the UII present lower values of 25 and 40, respectively. High *ATi* can indicate provenance signatures from silicic igneous rocks. However, apatite is susceptible to acidic leaching during weathering and diagenesis; therefore, a low *ATi* can often indicate either a highly weathered source, significant burial and dissolution, or subaerial exposure. Furthermore, the apatite's low durability can also decrease *ATi* by grain degradation during transport and injection.

The variability in the *X*-axis through all cross plots is controlled by the *GZi*. Domengine samples present the highest values, followed by an overlap between Kreyenhagen sandstones and the LII, while Lodo and the UII present the lowest values. High *GZi* can indicate input from metamorphic sources or deep diagenetic dissolution. Furthermore, hydraulic segregation can also influence this index due to contrasting densities between garnet and zircon.

Integrated analysis of these indices was made by PCA of indices centroids for all samples and Bayesian medians of main groups along with provenance similarity matrix based on standardized Euclidian distances and provenance similarity tree (Figure 9). The PCA of group medians (Figure 9B) shows strong affinity between Kreyenhagen channel-fills and intrusions. These groups present contrasting provenance signals with Lodo and more significantly with Domengine sandstones. The Lodo group shows negative values in both axis with opposite centroid distance from ATi, CZi and GZi and correlate with sandstone intrusions group with MZi and RZi centroids on PC1 axis. The Domengine group shows the strongest dissimilarity among indices centroids, with high positive values in PC1 and negative in the PC2 axis, with good correlation with CZi and GZi, which strongly correlates with metamorphic sources associated with mafic, ultramafic and high-grade metamorphic rocks. These relationships are demonstrated by the provenance similarity matrix where values between Kreyenhagen and intrusions are the lowest (Figure 9C) and by the Provenance similarity tree (Figure 9D).

4.4 | Assemblage Maturity Index (*ZTR*)

Assemblage maturity using *ZTR* was compared between parent units and intrusive sandstones in combination with *ATi* and *ZTi* indices with respective 90% confidence intervals (Figure 10). *ZTR* values observed in the LPU and LII indicate low maturity assemblages with values ranging from 10 to 35. The same is

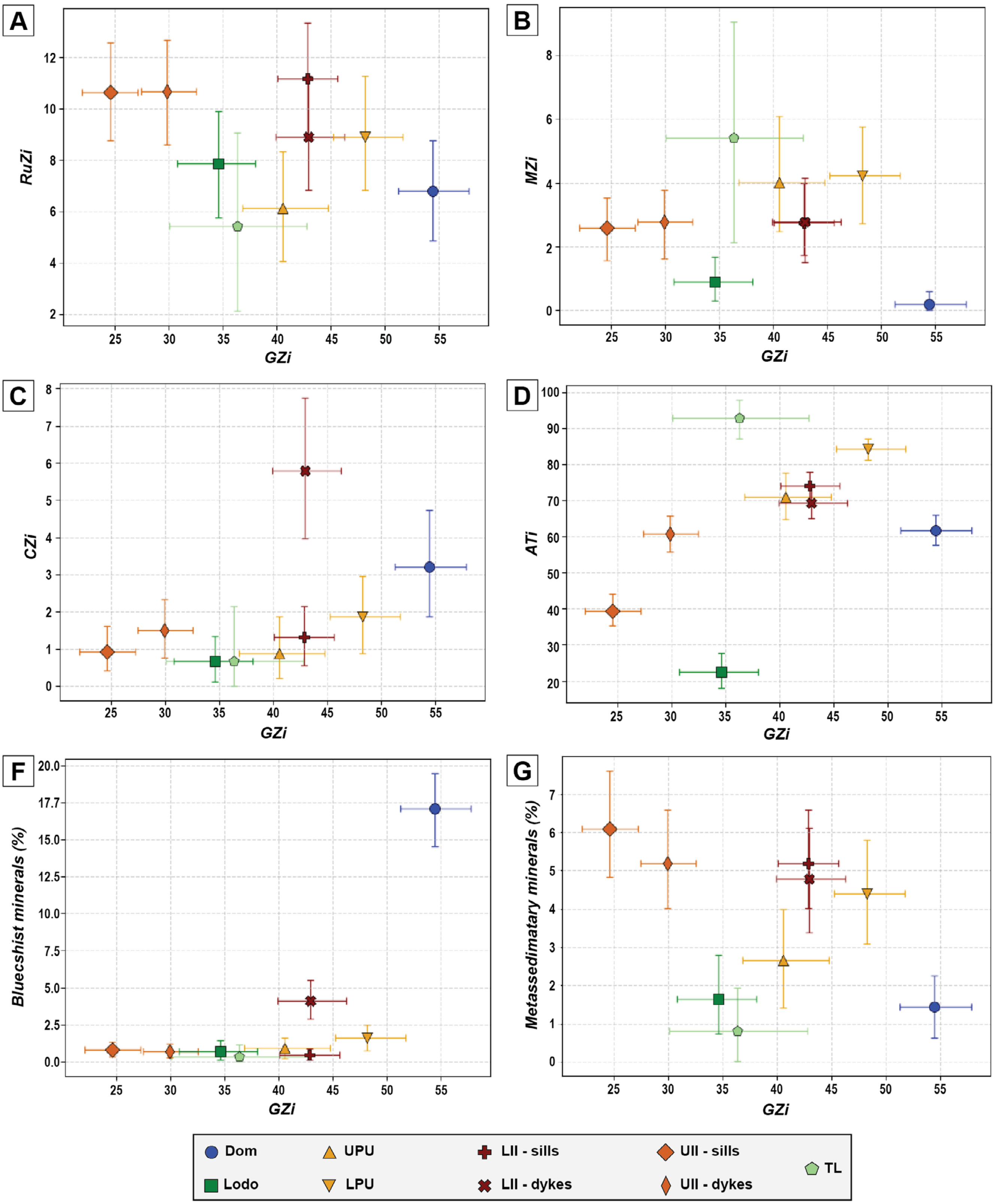

FIGURE 8 | Provenance-Sensitive Heavy Mineral Indices and mineral percentage cross-plots based on Bayesian Medians (index centroids) plotted with 90% Highest Density Intervals (HDI) as error bars. (A) *RuZi*; (B) *MZi*; (C) *CZi*; (D) *ATi*; (E) Blueschist minerals (glaucophane + lawsonite); (F) Metasedimentary minerals (kyanite + andalusite + staurolite). Inclusion of single samples from Tumey Sandstone Lentil for reference only. Values for A-D can be accessed in Table A6 and for F, G in Table A7 in the appendix.

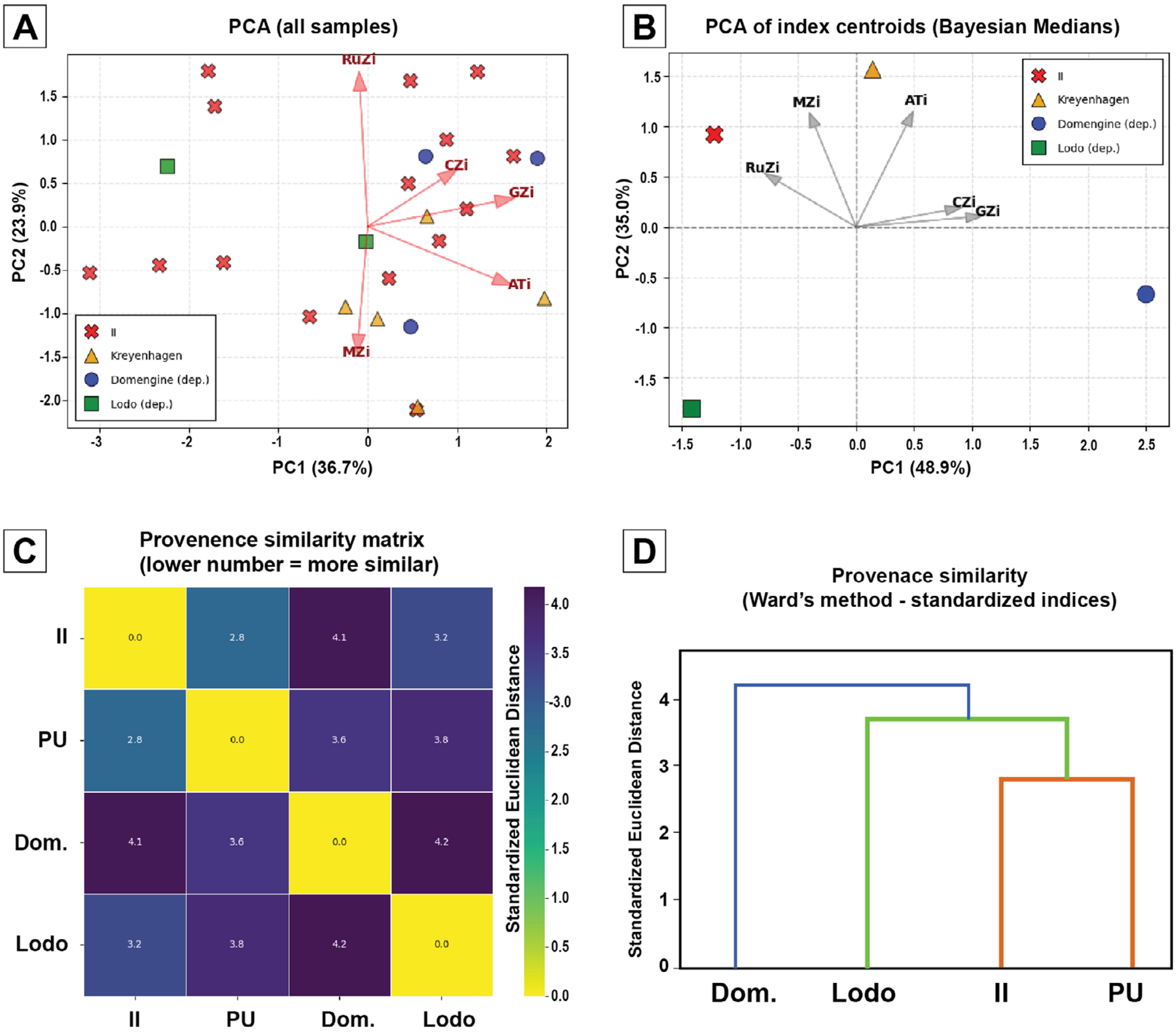

	II	PU	Dom.	Lodo
II	0.0	2.8	4.1	3.2
PU	2.8	0.0	3.6	3.8
Dom.	4.1	3.6	0.0	4.2
Lodo	3.2	3.8	4.2	0.0

FIGURE 9 | Provenance-sensitive indices analysis. (A) PCA of indices values for all samples. (B) PCA of index centroids (Bayesian Medians) of different units (Domengine, Lodo, Kreyenhagen, and injectite sandstones). Values can be accessed in Table A8 in the appendix. (C) Provenance similarity matrix based on Standardized Euclidean Distance. (D) Dendrogram of Provenance Index Similarities between groups constructed using Ward's method and Standardized Euclidean distance. Values in Table A9 of the appendix. Note best correlation exists between parent units and sandstone intrusions.

observed in the UPU and UII, except for the samples UI-03 and UI-129, which have values of 73 and 65 respectively, indicating relatively highly mature assemblages.

4.5 | Grain Degradation and Weathering Sensitive Index (*ATi*)

As apatite is a mechanical and chemical unstable mineral, it is contrasted with the ultrastable tourmaline to assess grain degradation and surface weathering within the complex (Figure 10). The lower channel-fills present coherent values narrowly ranging from 80 to 87 with median of 84. On the other hand, the LII present high variation with values ranging from 14 to 92 and lower median of 72. Similar behaviour is observed on the upper interval with UPU ranging from 62 to 76 (median = 70.8), and LII sandstone ranging from 0 to 94, with a sharp decrease in the median value to 48.8.

4.6 | Density Sensitive Index (*ZTi*)

The hydraulic segregation effects through TGIC were assessed by *ZTi* index, which compares proportions of minerals with contrasting densities (Figure 10). The LPU present consistent high ZTi values ranging from 80 to 85 (*av.* 82.5). In contrast, the LII shows scattered values ranging from 67 to 95, however with similar average to the LPU estimated in 82.7. When looking at the upper interval, the UPU showed values of 87 for the sample KS-04 and 98 for KS-06 averaging 92.5. The UII showed higher scattering of values, ranging from 66 to 97 and averaging 88.6.

When observing the samples from the wing-like intrusion in the UII, there is a progressive decrease in ZTi from the parent channel-fill (sample KS-06) to the intrusions (samples: UI-01, UI-02 and UI-03) showing a preferential settling of zircon grains in relation to lighter tourmaline.

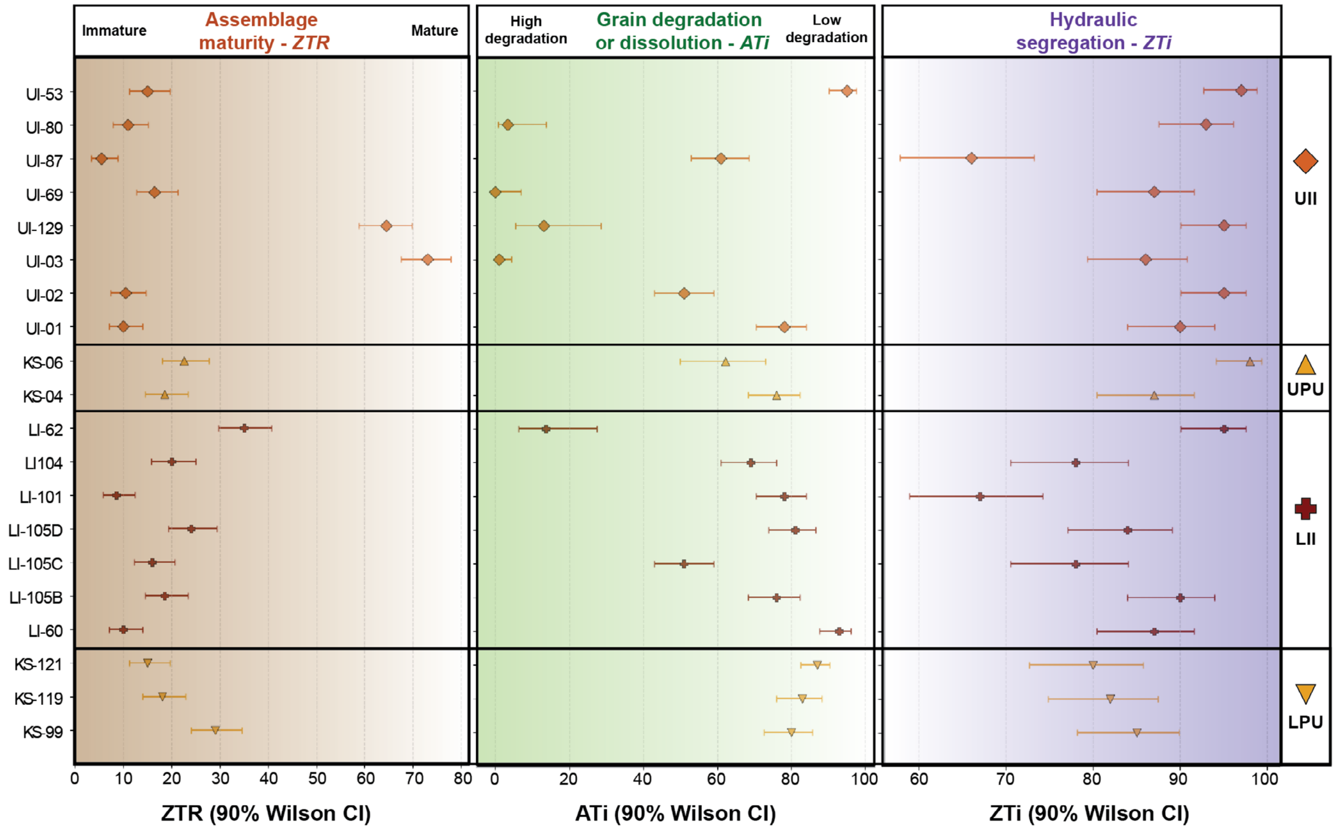

FIGURE 10 | Integrated analysis of assemblage maturity by ZTR (left), grain degradation and dissolution by ATi (centre), and hydraulic segregation by ZTi (right). Absolute values plotted with lower and upper 90% confidence intervals (Wilson's method) which can be accessed in Table A10 in the appendix.

4.7 | Microtextures

Qualitative petrographic analysis from SEM imaging was performed in the samples along the wing-like intrusion in the UII and its respective parent unit. Zircon grains from the channel-fill present varied morphologies including euhedral prismatic shapes with varied length: width ratios, angular broken grains, and rounded grains with internal zonation. Some grains have slightly rounded terminations, and linear fractures with minor pitting. Intrusions present grains that are more fragmented, commonly with sharp and jagged edges and intensely fractured surfaces (Figure 11). Tourmaline also records textural variations through the wing system. The parent unit either has prismatic, straight-sided grain morphologies, or occurs as broken fragments with sharp and angular corners. In the intrusions, angular to sub-rounded grains of platy tourmaline displaying irregular edges and fractured faces are observed.

Among less stable grains, garnet grains with intermediate hardness (h = 7) contain sub-rounded shapes with smooth surfaces in the parent unit and are more irregular and sub-angular along the wing. Staurolite (h = 7.25) exhibits fracture surfaces in all samples, but with distance away from the parent unit, fracture surfaces are more intense, and grain morphology is more irregular. Epidote and titanite have lower hardness (h = 6 and 5, respectively) and lack diagnostic characteristics that differentiate relative levels of textural modification among samples. These minerals preserve surface textures that are a combination of mechanical processes (fracturing and abrasion) and chemical modification, as shown by surface pitting caused by dissolution. Similar textures are developed in both the parent unit and the wing.

5 | Discussion

5.1 | Provenance of Depositional and Intrusive Sandstones

Detrital assemblages serve as provenance ‘fingerprints’ that enable differentiation and correlation of sandstone units (A. C. Morton 1985; Haughton et al. 1991; Mange-Rajetzky 1995). In this work, HMA was performed within sections where the intrusions have demonstrable spatial and genetic relationships with adjacent channel-fills (parent units) of Kreyenhagen Formation. However, the complex network of intrusions and the limitations of the rock exposures impose a higher degree of uncertainty on whether other stratigraphic intervals were involved in the TGIC development. Some examples are the depositional parent units that may occur and are not exposed, or local sand fluidization and remobilization from units that in outcrop are not deformed. Therefore, HMA was essential to track provenance signatures.

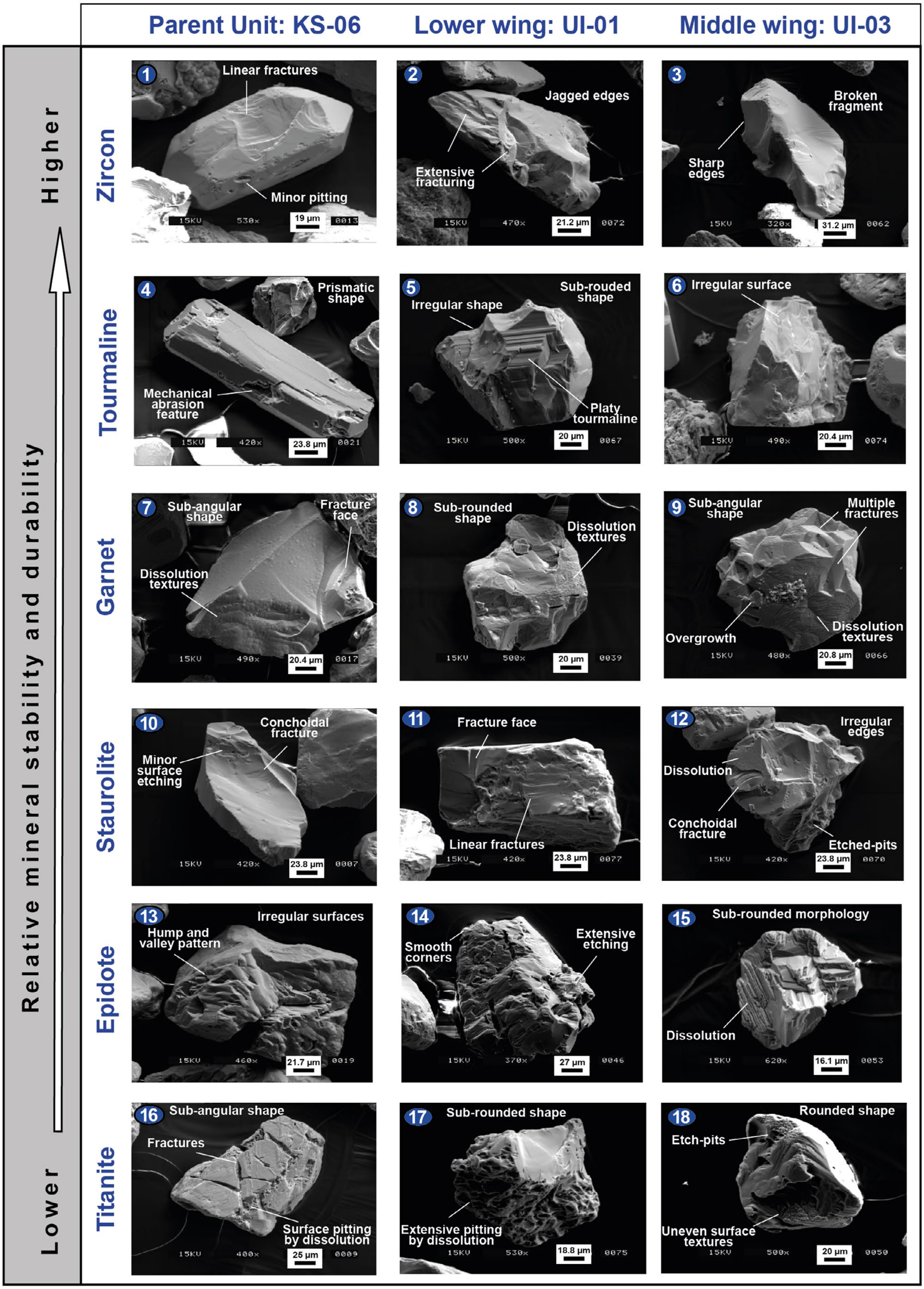

FIGURE 11 | SEM images showing microtextures of heavy minerals along the wing-like intrusion. Note relative increase of grain degradation from parent unit (sample KS-06) to intrusive network (UI-01 and UI-03).

5.1.1 | Depositional Units

As demonstrated through statistical analysis, the depositional sandstones from Lodo, Domengine, and Kreyenhagen formations contain distinctive HM assemblages, indicating changes in provenance and source-to-sink routes that are linked to intense tectonic activity and eustatic variations throughout the Paleogene (Figures 3 and 12).

The submarine fan deposits of Lodo Formation present two mineral parageneses. Zircon and titanite indicate granitic sources, whereas staurolite, andalusite, tourmaline, and some

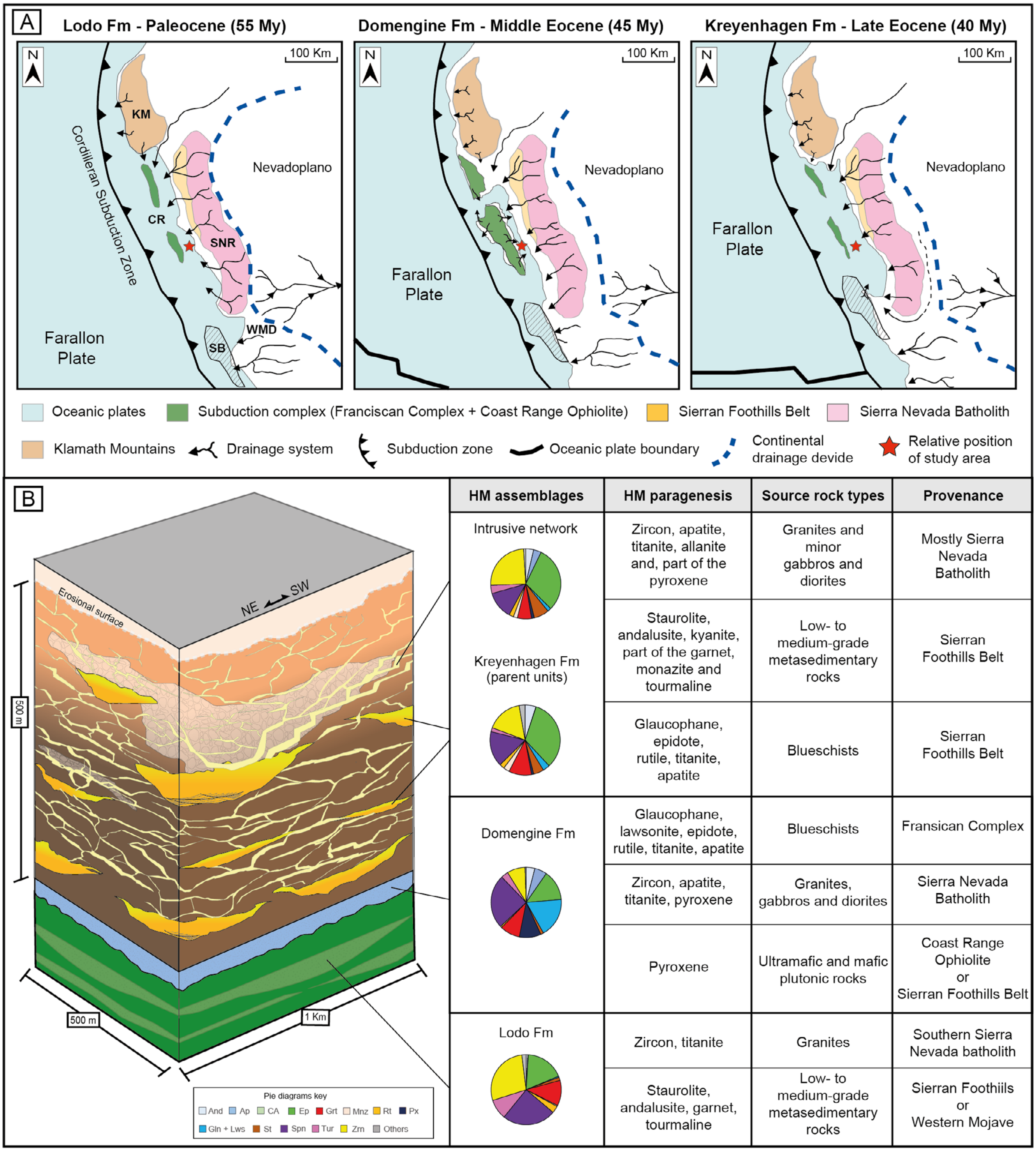

HM assemblages	HM paragenesis	Source rock types	Provenance
Intrusive network Kreyenhagen Fm (parent units)	Zircon, apatite, titanite, allanite and, part of the pyroxene	Granites and minor gabbros and diorites	Mostly Sierra Nevada Batholith
	Staurolite, andalusite, kyanite, part of the garnet, monazite and tourmaline	Low- to medium-grade metasedimentary rocks	Sierran Foothills Belt
	Glaucophane, epidote, rutile, titanite, apatite	Blueschists	Sierran Foothills Belt
Domengine Fm	Glaucophane, lawsonite, epidote, rutile, titanite, apatite	Blueschists	Fransican Complex
	Zircon, apatite, titanite, pyroxene	Granites, gabbros and diorites	Sierra Nevada Batholith
	Pyroxene	Ultramafic and mafic plutonic rocks	Coast Range Ophiolite or Sierran Foothills Belt
Lodo Fm	Zircon, titanite	Granites	Southern Sierra Nevada batholith
	Staurolite, andalusite, garnet, tourmaline	Low- to medium-grade metasedimentary rocks	Sierran Foothiils or Western Mojave

FIGURE 12 | Provenance analysis. (A) Paleogeographic reconstruction of the San Joaquin Basin during the deposition of the Lodo (Palaeocene), Domengine (Middle Eocene) and Kreyenhagen (Middle to Upper Eocene) formations. Modified after Bartow (1996) and Sharman et al. (2015). KM, Klamath Mountains; SNR, Sierra Nevada Range; WMD, West Mojave Desert; SB, Salinian Block; CR, coast range. (B) Pie charts illustrating the average heavy-mineral assemblage proportions for depositional and intrusive sandstones, including interpreted mineral paragenesis and inferred source units. Refer to Figure 6 for the heavy-mineral key.

of the garnet suggest metasedimentary origins (Figure 12). Petrographic analysis by Zvirtes et al. (2020) defined a tectonic provenance signature consistent with basement uplift. Paleocurrent data indicate a northward-prograding submarine fan system (Nilsen et al. 1974) developed during intense late Cretaceous–early Paleogene uplift of the southern Sierra Nevada, exposing granitic basement and supplying plutoniclastic detritus northward (Mitchell et al. 2010; R. V. Ingersoll 2012). The relatively simple provenance of Lodo Formation is also supported by calculated Shannon Entropy values; Lodo presented the lowest entropy of the depositional units examined (Figure 7B), indicating a restricted mineral source.

The shallow marine Domengine sandstones presented the most diverse HM assemblages (Figure 7) with mineral paragenesis indicating mixed source rocks. This mineral diversity is reflected by high Shannon Entropy values for this unit (Figure 7B). Zircon, apatite, titanite and some of the pyroxene grains can indicate derivation from granitic batholiths with associated granite, gabbro, and diorites. The other paragenesis is composed of glaucophane, lawsonite, epidote, apatite, and minor prehnite-pumpellyite and rutile, suggesting provenance from high-pressure metamorphic rocks (e.g., blueschists). This paragenesis can be attributed to detrital input from the Franciscan Complex to the west as suggested by petrological and paleocurrent data (Schulein 1993; Sharman et al. 2017; Zvirtes et al. 2020) (Figure 12). Furthermore, relatively high pyroxene content and CZi also indicate inputs from mafic or ultramafic sources, which is also abundant in the Franciscan Complex and Coast Range Ophiolite to the west. These western sources were exposed during the middle Eocene after a major relative sea-level fall, becoming a potential sediment supplier to the basin. The mixed provenance signatures suggest that the deltaic and estuarine depositional systems of Domengine were sourced from complex drainage systems and sediment catchment routes developed from east and west.

The assemblages of the Kreyenhagen Formation show low to moderate Shannon Entropy (Figure 7B), indicating more diverse sources than that of Lodo, but somewhat less fertile than Domengine. Three main HM paragenesis were defined for the Kreyenhagen Formation sandstones (Figure 12). An association of zircon, apatite, titanite, allanite, and pyroxene suggests granitic sources attributed to the Sierra Nevada batholith. Staurolite andalusite, kyanite, part of the garnet, monazite, and tourmaline indicate sources of low- to medium-grade metasedimentary rocks which can be assigned to the Sierran Foothills Belt located to the east and northeast of the area. The third paragenesis, composed of glaucophane, epidote, rutile, titanite, and apatite, suggests clastic input from blueschist-rich sources. This assemblage is likely derived from the Sierran Foothills Belt, to the east, which contains high-pressure metamorphic rocks from different accreted tectonic blocks (Snow and Scherer 2006). This provenance concurs with paleocurrent (Zvirtes et al. 2019) and geochronology data (Sharman et al. 2015), indicating westward sediment transport supplied from the Sierra Nevada. Alternatively, a Franciscan provenance is possible but less likely due to predominant westward sediment transport and the decrease or shutdown of sediment production and supply from the west controlled by the middle-to-Late Eocene transgression, submerging sources from the accretionary prism (Bartow 1991).

5.1.2 | Sandstone Intrusions

Assemblages from intrusions confirm the genetic relationship with the Kreyenhagen Formation. Both units present HM assemblages, mineral indices, and paragenesis from granitic and metamorphic rocks assigned to the Sierra Nevada batholith and Sierran Foothills Belt, respectively (Figure 12B). This relation is concordant to field observations and petrographic analysis where the channel-fills present westward sediment transportation from dissected magmatic arc signatures (Zvirtes et al. 2019, 2020) confirming Sierran sources. Shannon entropy of sandstone intrusions appears to be generally inherited from their associated Kreyenhagen parent units (Figure 7B).

The confirmation of the genetic link between the slope channel-fills of the Kreyenhagen Formation with no contribution from the underlying Lodo and Domengine sandstones demonstrates that injectites tend to develop through intraformational units rather than sediment fluidization from deeper units and intrusion across diverse formations. Similar context is reported in the older PGIC, in which the base-of-slope channels of the Dosados Sandstone (< 50 m thick) were confirmed to be the parent units for the complex based on HMA (Hurst et al. 2017). These units overlie the Panoche Formation, a much thicker succession (> 6 km thick) made of base-of-slope to basin plain fans and channel-fills (Vigorito et al. 2022). In subsurface, these interrelations are demonstrated in the North Sea, where the spatial link between parent units and sandstone intrusions is established. In the Greater Forties area (offshore UK), intrusions in the mudstone-prone Eocene are the overburden to the thick regionally developed aquifer in the Palaeocene Forties Formation (Van Oorschot et al. 2021). However, injected sediments were derived from immediately adjacent depositional sandstone rather than from the underlying Forties sandstone-rich units (Morton et al. 2014). In the Greater Alvheim area (offshore Norway), where large sandstone intrusions form oil reservoirs, the sand is derived from the thin underlying Hermod Sandstone rather than the regional Heimdal Formation (Luzinski et al. 2022).

5.2 | Processes Controlling HM Assemblages

A comprehensive assessment integrating hydraulic fractionation, grain degradation, diagenesis and surface weathering is essential to fully understand the processes controlling mineral assemblages and textures. As demonstrated, HM assemblages of the TGIC vary from parent units to intrusive network. Shannon Entropy values indicating assemblages both *more* and *less* diverse occur in injectites, compared to their parent units (Figure 7B). This suggests that geological processes related to syn- and post-sand emplacement could have modified the composition and texture of these rocks. Here we discuss each of these processes and the interlinks between them.

5.2.1 | Hydraulic Segregation

The sorting of detrital grains is considered to be governed by grain size, shape and density and the response to active processes during erosion, transportation and deposition (Komar 2007;

Garzanti et al. 2008). The higher densities and generally finer grain sizes make heavy minerals more resistant to entrainment by flowing water, consequently having lower rates of transport when carried as part of the bedload or in suspension where differences in grain settling velocities are important. The same principle is here applied to the TGIC, where overpressure is released by a chain of processes that promote widespread seal breaching through hydrofractures, sand fluidization, and injection through > 400 m mudstone strata. With this scenario, variations in fluid conditions such as flow velocity, pressure, and rheology throughout sediments' trajectories during injection across complex labyrinths of fractures are expected to promote hydraulic sorting.

As demonstrated by the ZTi, processes of hydraulic segregation from parent units to sandstone intrusions are suggested.

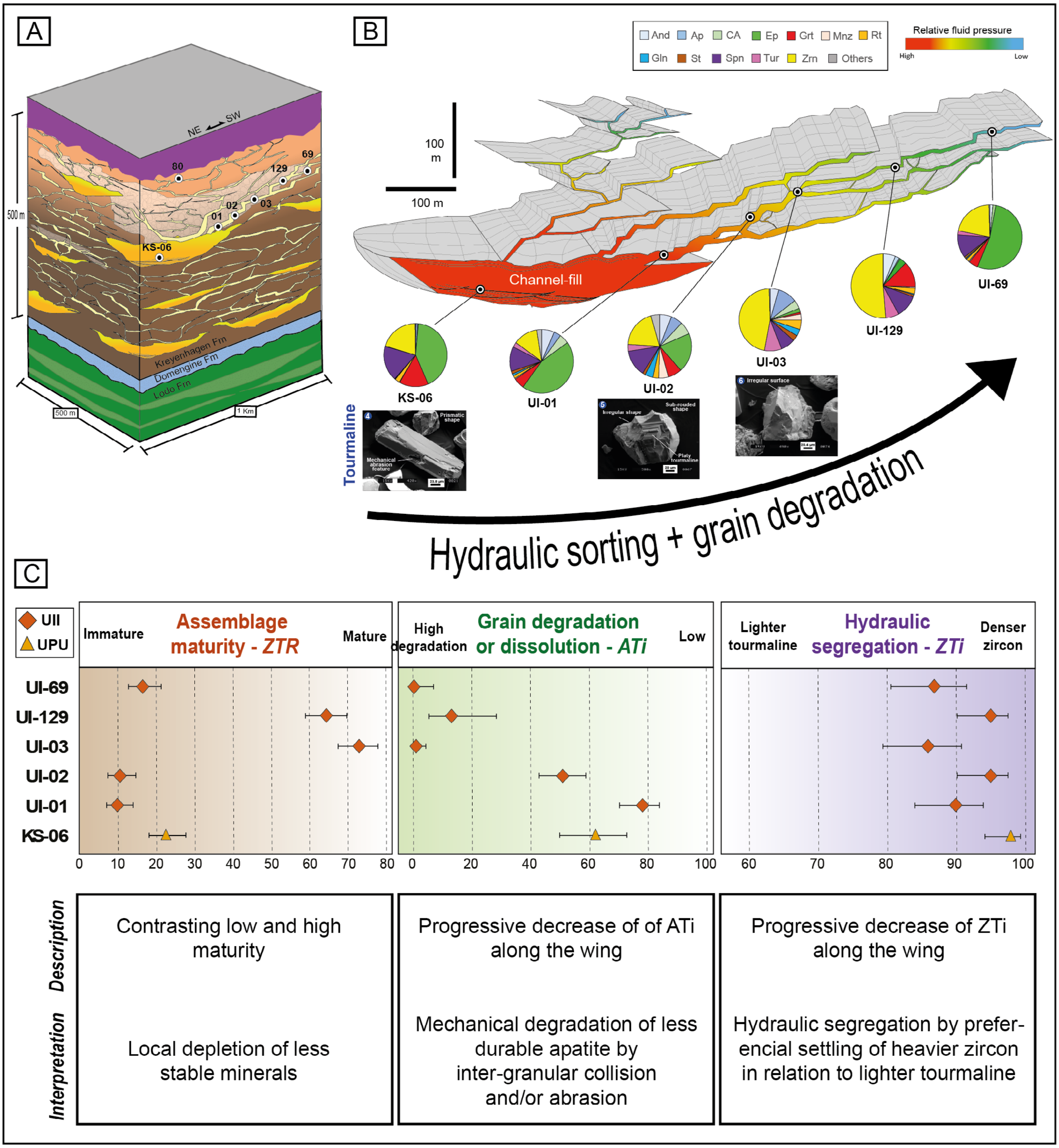

Contrasting low and high maturity

Local depletion of less stable minerals

Progressive decrease of of ATi along the wing

Mechanical degradation of less durable apatite by inter-granular collision and/or abrasion

Progressive decrease of ZTi along the wing

Hydraulic segregation by preferencial settling of heavier zircon in relation to lighter tourmaline

FIGURE 13 | (A) Block diagram illustrating the architecture of the TGIC and the relative sampling locations along the structure. (B) Simplified conceptual model of the "wing" displaying heavy-mineral (HM) assemblage proportions for each sample and SEM images of HM grains. Refer to Figure 6 for the HM key. (C) Integrated analysis of the wing-like intrusion system, showing mineral maturity (ZTR index), grain degradation/dissolution (ATi) and hydraulic segregation (ZTi) trends (top) with respective description and interpretation.

This is particularly observed in the wing-like intrusion where ZTi tends to decrease along the structure (Figure 13). This behaviour suggests gravitational settling of heavier zircon grains in relation to lighter tourmaline by variable sustained periods of fluid flow along with progressive drops in fluid pressure and flow velocity during injection. When directly analysing the percentage of zircon, the preferential settling is confirmed by the increase in zircon quantities marked by the samples UI-02 and UI-03. Similar trends are recorded from the Panoche Giant Injection Complex (cf. Hurst et al. 2017; Figure 3).

5.2.2 | Grain Degradation During Injection

The mechanical stability of HM plays a crucial role on the distribution, degree of preservation, and textures of sediments during sedimentary transport (Thiel 1945). Minerals highly resistant to mechanical abrasion, fracturing, diagenesis, and weathering, such as zircon, rutile, and tourmaline, tend to retain their primary morphological characteristics throughout the sedimentary cycle (Mange and Wright 2007). In contrast, less stable minerals, such as apatite, titanite and epidote, are more susceptible to comminution during transport and mechanical compaction during burial.

The low ZTR from parent units and most of the intrusive sandstones characterize the assemblages as highly immature. The exception is the samples UI-03 and UI-129 representing the upper sections of the wing-like intrusion (Figure 13). The question is—why do these samples present high ZTR? In order to respond to that, we have to gather information from other parameters to propose plausible hypotheses.

The spike on ZTR means that the assemblages are depleted in less stable minerals. If these results are not caused by occasional sampling of levels concentrated in more stable minerals, this depletion could be potentially caused by preferential grain degradation of lower-stability minerals. If that is the case, what are the processes that could have induced this degradation? Was it the preferential 'erosion' of less stable grains by inter-granular interactions during sand injection emplacement, such as high-velocity collision or grain-to-grain grinding and shearing? Or were the post-emplacement processes associated with burial (compaction and dissolution) and exhumation (surface weathering) the main controls on the degradation of less stable and less durable minerals?

To answer these questions, *ZTR* with *ATi values* were compared, as these indices give information on assemblages maturity and degree of grain degradation, respectively. As apatite has extremely low hardness, it can be quickly degraded by mechanical erosion. However, apatite is also highly reactive with acidic fluids that are common in surface weathering (meteoric water). The *ATi* values between parent units and intrusive intervals show a relatively similar pattern to *ZTR* where samples in general present high *ATi*, indicating preservation of less durable apatite within immature assemblages. However, in the UII, there is a progressive decrease of *ATi* along the wing, especially marked by the samples UI-03, UI-129 and UI-69.

If the cause for the depletion on less stable minerals, indicated by high *ZTR* and low *ATi* values, was dissolution by diagenesis or surface weathering, we would expect the depletion to be expressed throughout both depositional and intrusive units, which is not the case. There is, therefore, a good scenario to correlate this variation to mechanical degradation of grains. In this case, there are two possible hypotheses. One would be mechanical compaction after sand emplacement, leading to grain degradation of softer minerals. However, the effect of compaction would also be expected to be more homogeneous throughout the complex; therefore, not considered a major mechanism. The second is the inter-granular interactions during sand fluidization and injection, promoting grain collisions or grain-to-grain grinding and shearing. This process could explain the variations in both indices and the grain microfracturing and breakage observed in Figure 13. Grain microfracturing damage from the wing at Tumey Hills was also reported in Zvirtes et al. (2020) where quantitative analyses of fractures in the framework grains showed an increase in fractured grains from 5% to 10% in the parent channel-fill to 30% in some of the intrusions.

Mechanical attrition of grains and abrasion has also been reported and interpreted to be sustained during sand injection (Scott et al. 2009; Bouroullec and Pyles 2010; Hurst et al. 2017). However, the nature of fluid dynamics during sand injection remains debated. Some authors suggested a predominantly high-velocity, dilute, and turbulent flow regime (Vigorito et al. 2008; Scott et al. 2009; Vigorito and Hurst 2010; Ross et al. 2014; Zvirtes et al. 2020), while others propose that a laminar flow regime is dominant, with low-velocity, high-density suspensions or granular flows (slurries) being the main types of flow (Sherry et al. 2012; Cobain et al. 2015; Kelly and Brettle 2024). Other studies have suggested that flow may be initially turbulent during hydrofracture propagation and later become laminar as the fracture closes or flow decelerates (Dodd et al. 2019). We consider a dynamic scenario for the TGIC where variation in fluid characteristics and flow conditions intensely changes at various stages of the sand emplacement. At early stages, hydrofracturing of host mudstones is followed by fluid escape, sand fluidization and injection under highly unstable and turbulent flow conditions where inter-granular collisions can occur (Scott et al. 2009; Zvirtes et al. 2019; Hurst et al. 2021; Luzinski et al. 2022). As injection emplacement proceeds, the fluid (water and sediments) increases grain concentration and decreases velocity, promoting granular flow (slurry) conditions. This can induce grain-to-grain interaction, which may also promote grain degradation and microfracturing. Given its complexities, emplacement of SICs must involve varied flow dynamics within a network of propagating fractures, where variations in pressure, fluid character and flow velocities at various stages are expected.

5.2.3 | Diagenesis and Surface Weathering

Once injectites are emplaced, they form active permeable conduits for fluid flow, allowing intrusions to continue transmitting fluids post-injection (Jonk 2010; Vigorito and Hurst 2010). Highly permeable intrusive networks enhance fluid migration, which may either promote diagenetic cementation or lead to mineral dissolution during deep weathering (Hurst et al. 2017; Figure 13).

Effects of diagenetic processes and surface weathering were assessed through HM assemblages, mechanical and chemical sensitive indices (*ZTR* and *ATi*), and microtextures through SEM images. Parent units and intrusive sandstones showed immature assemblages with low *ZTR* and a relative preservation of very unstable apatite with high *ATi*. To preserve low stability and low durability grains in the channel-fills, we have to assume that: (1) the sediment input from source terrenes was relatively close to the depositional environment, (2) no major weathering along the transport history of detritus and (3) once deposited, sediments were not buried to deep depths. Although evidence of chemical modification is present in the TGIC, all samples remain moderately to poorly consolidated and have not been subjected to burial temperatures exceeding 40°C–45°C (equivalent to ~1 to 1.5 km depth), given a geothermal gradient of 25°C–30°C/km (Vigorito et al. 2024). Consequently, most preserved dissolution features are attributed to surface weathering rather than burial diagenesis. Zvirtes et al. 2020 reported important compaction in the parent channel-fill and to a lesser extent in the intrusive sandstones where soft platy micas (biotite and muscovite) and mudstone clasts are deformed within tight grain-to-grain contacts. However, we believe that this could be a subordinate process to explain the variations in ATi and ZTR values throughout the complex. Furthermore, pervasive gypsum cementation of both parent units and intrusions prevented further compaction and preserved unstable HM from surface weathering. This scenario offers the opportunity to assess low durability minerals, like apatite, as mechanically soft minerals that can respond to grain degradation by mechanical erosion rather than chemical dissolution.

Calculated values of Shannon Entropy were challenging to interpret in context of weathering and diagenesis. As stated before, Shannon Entropy measures diversity of the assemblage; this should be a great proxy for maturity of the sediment, as weathering and diagenesis are known to decrease mineral diversity (e.g., Morton and Hallsworth 1999). However, low Shannon Entropy (low diversity) could also be indicative of low diversity of HM in the source area. This seems to be the case here. Some of the lowest Shannon Diversities were observed for the intrusive intervals and parent units (Figure 7B), and many of samples derived from these units preserve significant amounts of titanite and epidote (Figure 5), which are known to be extremely unstable in burial diagenesis (Morton and Hallsworth 1999).

5.3 | Implications for Subsurface

Injectites can deeply influence the architecture and properties of hydrocarbon reservoirs, such as in the North Sea, where they are recognized as key reservoir components based on interpretations of seismic and well data used for exploration and production (Dixon et al. 1995; MacLeod et al. 1999; Lonergan et al. 2000; Hurst et al. 2003; Huuse et al. 2005; De Boer et al. 2007; and references therein). Application of HMA in subsurface, where injectites were present but not considered, focused initially on the lithostratigraphy of depositional hydrocarbon reservoirs in which sedimentologic and biostratigraphic data produced inadequate reservoir correlation (e.g., Hurst and Morton 1988; Mange-Rajetzky 1995; Morton and Hurst 1995). Subsequent applications to reservoirs associated with sand injection complexes proved successful in supporting reservoir correlation and establishing connectivity relationships between intrusions and parent units (e.g., Poulsen et al. 2007; Morton et al. 2014; Luzinski et al. 2022). Most recently, HMA has been leveraged to differentiate sandstones remobilised in situ (originally depositional) from those fully injected (Luzinski et al. 2025). Although their approach still relied on correlation and comparison of suspected depositional and intrusive sandstones in proximity of the studied section, it paves way to practical application of HMA-based sand injection diagnostics, which have so far only been theorized (Hurst et al. 2021).

Outcrop analogue data from well-exposed, km-scale exposures, help interpretations of injectites in subsurface because physical relationships among sandstones are visible and predominantly unambiguous (e.g., Grippa et al. 2019; Zvirtes et al. 2019; Vigorito et al. 2022, 2024; Surlyk et al. 2007; Andrews et al. 2026). Therefore, based on the learnings from the HMA here presented, a conceptual analogy for inter-borehole correlation using pseudo-well sections from TGIC outcrop data is presented in Figure 14. Hypothetical HMA results from the four wells show mineralogical variations among samples (Figure 14A). A possible sedimentological interpretation suggests that these differences reflect a series of stacked, laterally migrating slope channel-fills, where provenance signatures shifts or variations in the sedimentary routing system are recorded throughout the succession (Figure 14B). This interpretation implies limited lateral reservoir continuity and poor connectivity, reducing reserve estimates. Alternatively, the identification of a common provenance signature, combined with HM assemblages variations on specific minerals and textures linked to sand injection processes supports an injectite interpretation (Figure 14C). In this example, outcrop data from the TGIC wing confirm the correct interpretation and correlation. If these pseudo-wells represented real subsurface data, then a depositional model might have prevailed, potentially leading to negative outcomes for field exploration.

6 | Conclusions

The integrated field mapping and heavy mineral analysis of the Tumey Giant Injection Complex provided important petrological information for understanding part of the source-to-sink dynamics of the forearc San Joaquin basin during the Paleogene and the evolution of the injection complex. Statistical characterization of heavy mineral assemblages, supported by Bayesian modelling and multivariate analysis, confirms that the TGIC was primarily sourced from the slope channel-fills of the Kreyenhagen Formation. These parent units represent a dominant westward sediment routing from the Sierra Nevada province. In contrast, the underlying Domengine Formation preserves a distinct mixed-provenance signature, including diagnostic glaucophane and lawsonite, revealing a significant detrital contribution from the uplifted Franciscan Complex accretionary prism to the west.

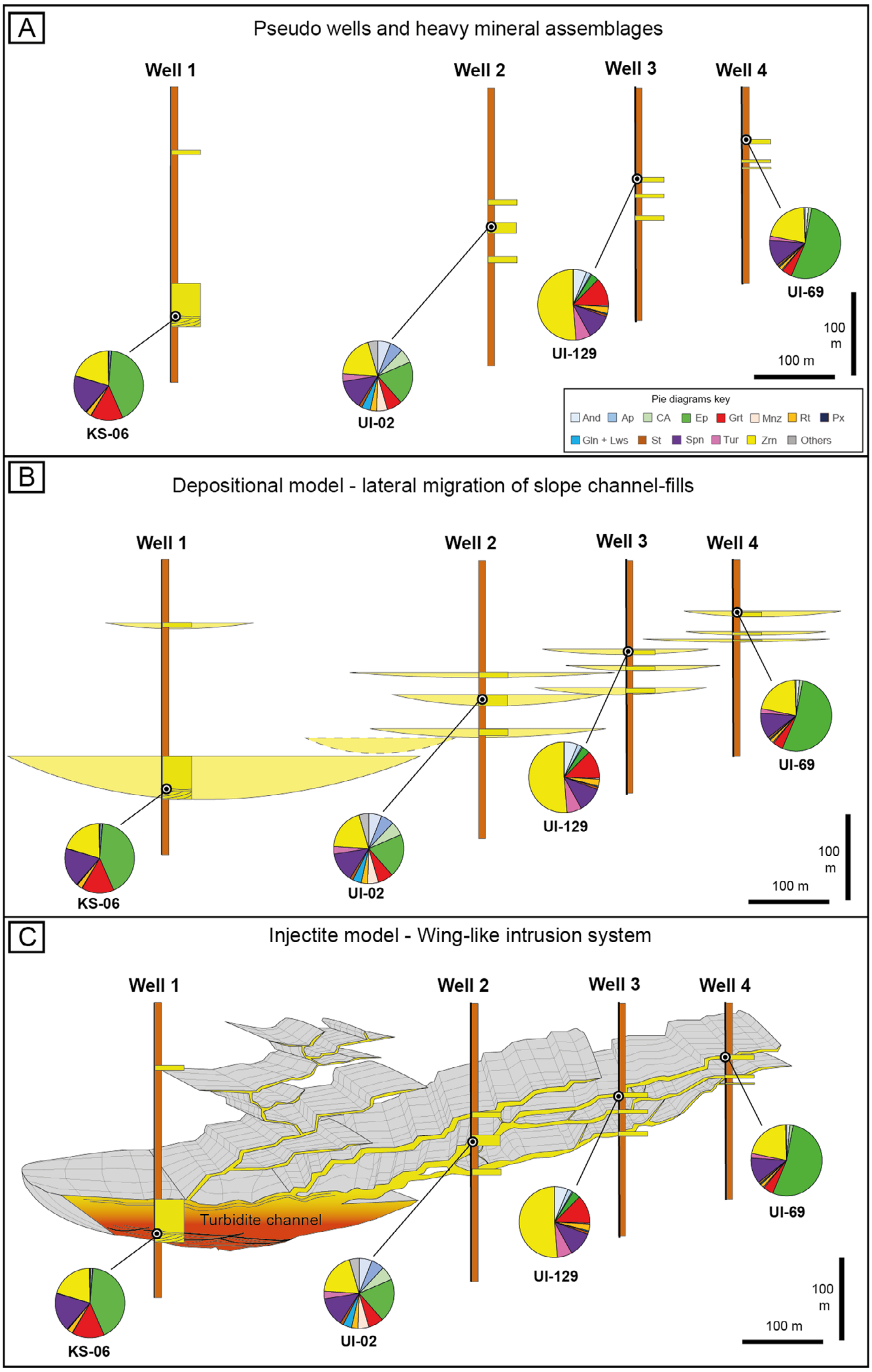

FIGURE 14 | Lithostratigraphic correlation and interpretation from hypothetical well data and heavy mineral assemblages. (A) Logs and heavy mineral assemblages (pie diagrams) from sandstone units. (B) Possible depositional models with levels vertical and lateral migration of channel-fills. (C) Actual injectite model from wing-like intrusion of TGIC with variation in heavy mineral assemblages associated with hydraulic fractionation and grain degradation.

Beyond provenance identification, this study demonstrates that the petrological evolution of SICs is affected by mechanical and hydraulic processes during sediment fluidization and emplacement. The observed depletion of unstable minerals (low *AT*i) and the corresponding spike in ultrastable phases (high *ZTR*) along a km-scale wing-like intrusion are interpreted as evidence of mechanical grain degradation. This interpretation is reinforced by SEM microtextural analysis, which reveals a higher degree of grain fracturing and degradation in the intrusions compared to their parent channel-fill. These findings suggest inter-granular interactions in response to dynamic and variable fluid flow properties and hydrodynamic conditions during sand injection emplacement. These processes can fundamentally alter the mineralogical maturity of a sandstone, potentially decoupling it from its original primary parent unit signature.

The TGIC further serves as a natural example of hydraulic segregation in injectite systems. The systematic variation in the density-sensitive *ZTi* index along the wing architecture reveals that heavy minerals respond to the fluid dynamics of injection. The progressive settling of denser zircon grains relative to tourmaline as sand moves away from the parent unit suggests syn-injection density-driven sorting. This confirms that injectite networks behave as hydrodynamic conduits, where fluctuations in flow velocity and pressure gradients modify the spatial distribution of mineral phases.

Finally, the results of this study have significant implications for the characterization of sand injection complexes in the subsurface, where complex 3D architectures cannot be fully resolved due to limitation in seismic resolution and wellbore data. By utilizing the specific mineralogical and textural 'fingerprints' of injectites, such as provenance signatures, mechanical degradation, and hydraulic sorting trends, we can better evaluate interlinks between depositional units and intrusive networks. The methodology presented here provides a robust tool for lithostratigraphic correlation, supporting alternative geological concepts, and improving our understanding of sediment routing and processes in sedimentary basins associated to SICs.

Acknowledgements

The authors gratefully acknowledge the support of the Sand Injection Research Group (SIRG) and its Phase 5 consortium member companies. We also thank CNPq and ANP (Agencia Nacional do Petróleo) for their support through the 'UoA-UFRGS-SWB Sedimentary Systems project. We extend our sincere thanks to the Guest Editor, Bryan Cronin, for his expert handling of the submissions for this special issue, which significantly enhanced the quality and cohesion of the thematic collection. We are also grateful to the Bureau of Land Management (BLM-California) for their essential collaboration in granting permissions and facilitating field access. Finally, we thank Raymond Ingersoll, David Hodgson, Glen Sharman, and Ben Callow for their insightful reviews and constructive comments.

Funding

The authors have nothing to report.

Conflicts of Interest

The authors declare no conflicts of interest.

Data Availability Statement

The data that support the findings of this study are available from the corresponding author upon reasonable request.

Peer Review

For transparency, the peer review documents associated with this article are available at https://doi.org/10.1111/bre.70107.

References

Aitchison, J. 1983. "Principal Component Analysis of Compositional Data." *Biometrika* 70, no. 1: 57–65.

Aitchison, J. 1986. *The Statistical Analysis of Compositional Data*. Chapman and Hall.

Allen, P. A. 2008. "From Landscapes Into Geological History." *Nature* 451, no. 7176: 274–276. https://doi.org/10.1038/nature06586.

Andrews, S. D., E. Keavney, D. M. Hodgson, et al. 2026. "Giant Injectite Complex Sand Body Architecture in the Late Jurassic East Greenland Rift." *Journal of the Geological Society* 183, no. 2: jgs2025-144. https://doi.org/10.1144/jgs2025-144.

Atwater, T. 1970. "Implications of Plate Tectonics for the Cenozoic Tectonic Evolution of Western North America." *GSA Bulletin* 81: 3513–3536.

Bartow, J. A. 1991. "Cenozoic Evolution of the San Joaquin Valley, California." *U.S. Geological Survey Professional Paper* 1501: 1–40.

Bartow, J. A. 1996. "Geologic Map of the West Border of the San Joaquin Valley in the Panoche Creek-Cantua Creek Area, Fresno and San Benito Counties, California." *U.S. Geological Survey Miscellaneous Investigations Series Map*, I-2430, 1 Sheet, Scale 1:50,000.

Bird, P., and R. V. Ingersoll. 2022. "Kinematics and Paleogeology of the Western United States and Northern Mexico Computed From Geologic and Paleomagnetic Data." *Ma: Geosphere* 18: 1563–1599. https://doi.org/10.1130/GES02474.1.

Bouroullec, R., and D. R. Pyles. 2010. "Sandstone Extrusions and Slope Channel Architecture and Evolution: Mio-Pliocene Monterey and Capistrano Formations, Dana Point Harbor, Orange County, California, U.S.A." *Journal of Sedimentary Research* 80, no. 5: 376–392. https://doi.org/10.2110/jsr.2010.043.

Brown, L. D., T. T. Cai, and A. DasGupta. 2001. "Interval Estimation for a Binomial Proportion." *Statistical Science* 16, no. 2: 101–133.

Caracciolo, L. 2020. "Sediment Generation and Sediment Routing Systems From a Quantitative Provenance Analysis Perspective: Review, Application and Future Development." *Earth-Science Reviews* 209: 103226.

Cartwright, J., M. Huuse, and A. Aplin. 2007. "Seal Bypass Systems." *AAPG Bulletin* 91, no. 8: 1141–1166. https://doi.org/10.1306/04090705181.

Chayes, F. 1960. "On Correlation Between Variables of Constant Sum." *Journal of Geophysical Research* 65, no. 8: 2419–2433.

Cobain, S. L., D. M. Hodgson, J. Peakall, and M. N. Shiers. 2017. "An Integrated Model of Clastic Injectites and Basin Floor Lobe Complexes: Implications for Stratigraphic Trap Plays." *Basin Research* 29, no. 6: 816–835.

Cobain, S. L., J. Peakall, and D. M. Hodgson. 2015. "Indicators of Propagation Direction and Relative Depth in Clastic Injectites: Implications for Laminar Versus Turbulent Flow Processes." *Geological Society of America Bulletin* 127, no. 11–12: 1816–1830.

Davis, J. C. 2002. *Statistics and Data Analysis in Geology*. 3rd ed. Wiley.

De Boer, W., P. B. Rawlinson, and A. Hurst. 2007. "Successful Exploration of a Sand Injectite Complex: Hamsun Prospect, Norway Block 24/9." In *Sand Injectites: Implications for Hydrocarbon Exploration and Production: American Association of Petroleum Geologists Memoir*, edited by A. Hurst and J. Cartwright, 65–68. American Association of Petroleum Geologists.

DeGraaff-Surpless, K., S. A. Graham, J. L. Wooden, and M. O. McWilliams. 2002. "Detrital Zircon Provenance Analysis of the Great Valley Group, California: Evolution of an Arc-Forearc System." *Geological Society of America Bulletin* 114: 1564–1580.

Dickinson, W. R., and E. Rich. 1972. "Petrologic Intervals and Petrofacies in the Great Valley Sequence, Sacramento Valley, California." *GSA Bulletin* 83: 3007–3024.

Dickinson, W. R., and D. R. Seely. 1979. "Structure and Stratigraphy of Forearc Regions." *AAPG Bulletin* 63: 2–31.

Dixon, R. J., K. Schofield, R. Anderton, et al. 1995. “Sandstone Diapirism and Clastic Intrusion in the Tertiary Submarine Fans of the Bruce-Beryl Embayment, Quadrant 9, UKCS.” *Geological Society, London, Special Publications* 94: 77–94.

Dodd, T. J. H., D. J. McCarthy, and S. M. Clarke. 2019. “Clastic Injectites, Internal Structures and Flow Regime During Injection: The Sea Lion Injectite System, North Falkland Basin.” *Sedimentology* 67: 1014–1044. https://doi.org/10.1111/sed.126722.

Duranti, D., and A. Hurst. 2004. “Fluidization and Injection in the Deep-Water Sandstones of the Eocene Alba Formation (UK North Sea).” *Sedimentology* 51, no. 3: 503–529. https://doi.org/10.1111/j.1365-3091.2004.00634.x.

Garzanti, E., S. Andò, and G. Vezzoli. 2008. “Settling Equivalence of Detrital Minerals and Grain-Size Dependence of Sediment Composition.” *Earth and Planetary Science Letters* 273, no. 1–2: 138–151. https://doi.org/10.1016/j.epsl.2008.06.020.

Gelman, A., J. B. Carlin, H. S. Stern, D. B. Dunson, A. Vehtari, and D. B. Rubin. 2013. *Bayesian Data Analysis*. 3rd ed. CRC Press.

Giannetta, L. G., and R. J. Behl. 2022. “Chemostratigraphic and Lithostratigraphic Framework of the Eocene Kreyenhagen Formation, Kettleman Area, Central San Joaquin Basin, California.” *Understanding the Monterey Formation and Similar Biosiliceous Units Across Space and Time* 556: 273–300. https://doi.org/10.1130/2022.2556(12).

Graham, S. A. 1978. “Role of Salinian Block in Evolution of San Andreas Fault System, California.” *AAPG Bulletin* 62: 2214–2231. https://doi.org/10.1306/c1ea53c3-16c9-11d7-8645000102c1865d.

Grippa, A., A. Hurst, G. Palladino, D. Iacopini, I. Lecomte, and M. Huuse. 2019. “Seismic Imaging of Complex Geometry: Forward Modeling of Sandstone Intrusions.” *Earth and Planetary Science Letters* 513: 51–63. https://doi.org/10.1016/j.epsl.2019.02.011.

Haughton, P. D. W., S. P. Todd, and A. C. Morton. 1991. “Sedimentary Provenance Studies.” In *Developments in Sedimentary Provenance Studies*, edited by A. C. Morton, S. P. Todd, and P. D. W. Haughton, vol. 57, 1–11. Geological Society, London, Special Publications. https://doi.org/10.1144/GSL.SP.1991.057.01.01.

Hubert, J. F. 1962. “A Zircon–Tourmaline–Rutile Maturity Index and the Interdependence of the Composition of Heavy Mineral Assemblages With the Gross Composition and Texture of Sandstones.” *Journal of Sedimentary Petrology* 32: 440–450.

Hurst, A., J. A. Cartwright, M. Huuse, et al. 2003. “Significance of Large-Scale Sand Injectites as Long-Term Fluid Conduits: Evidence From Seismic Data.”

Hurst, A., J. A. Cartwright, M. Huuse, and D. Duranti. 2006. “Extrusive Sandstones (Extrudites): A New Class of Stratigraphic Trap?” In *The Deliberate Search for the Stratigraphic Trap*, edited by M. R. Allen, G. P. Goffey, R. K. Morgan, and I. M. Walker, vol. 254, 289–300. Geological Society, London.

Hurst, A., W. Luzinski, G. Zvirtes, et al. 2021. “Some Petrographic and Mineralogical Diagnostics of Sandstone Intrusions.” *Geological Society, London, Special Publications* 493, no. 1: 287–302. https://doi.org/10.1144/sp493-2018-063.

Hurst, A., A. Morton, A. Scott, M. Vigorito, and D. Frei. 2017. “Heavy-Mineral Assemblages in Sandstone Intrusions: Panoche Giant Injection Complex, California, U.S.A.” *Journal of Sedimentary Research* 87, no. 4: 388–405. https://doi.org/10.2110/jsr.2017.22.

Hurst, A., and A. C. Morton. 1988. “An Application of Heavy-Mineral Analysis to Lithostratigraphy and Reservoir Modelling in the Oseberg Field, Northern North Sea.” *Marine and Petroleum Geology* 5: 157–170.

Hurst, A., A. Scott, and M. Vigorito. 2011. “Physical Characteristics of Sand Injectites.” *Earth-Science Reviews* 106: 215–246. https://doi.org/10.1016/j.earscirev.2011.02.004.

Huuse, M., J. A. Cartwright, R. Gras, and A. Hurst. 2005. “Kilometre-Scale Sandstone Intrusions.” In *Petroleum Geology: North-West Europe and Global Perspectives—Proceedings of the 6th Petroleum Geology Conference*, edited by A. G. Dore ´ and B. A. Vinning, 1577–1594. Petroleum Geology. Conferences Ltd. Published by the Geological Society.

Ingersoll, R. V. 1978. “Petrofacies and Petrologic Evolution of the Late Cretaceous Fore-Arc Basin, Northern and Central California.” *Journal of Geology* 86, no. 3: 335–352. https://doi.org/10.1086/649695.

Ingersoll, R. V. 1979. “Evolution of the Late Cretaceous Forearc Basin, Northern and Central California: Geological Society of America Bulletin, v. 90.” *Part* 1: 813–826.

Ingersoll, R. V. 1983. “Petrofacies and Provenance of Late Mesozoic Forearc Basin, Northern and Central California.” *AAPG Bulletin* 67: 1125–1142.

Ingersoll, R. V. 2012. “Composition of Modern Sand and Cretaceous Sandstone Derived From the Sierra Nevada, California, USA, With Implications for Cenozoic and Mesozoic Uplift and Dissection.” *Sedimentary Geology* 280: 195–207. https://doi.org/10.1016/j.sedgeo.2012.03.022.

Johnson, C. L., and S. A. Graham. 2007. “Middle Tertiary Stratigraphic Sequences of the San Joaquin Basin, California.” In *Petroleum Systems and Geologic Assessment of Oil and Gas in the San Joaquin Basin Province*, edited by A. H. Scheirer, 1713. California.

Jonk, R. 2010. “Sand-Rich Injectites in the Context of Short-Lived and Long-Lived Fluid Flow.” *Basin Research* 22: 603–621. https://doi.org/10.1111/j.1365-2117.2010.00471.x.

Kelly, S., and M. Brettle. 2024. “Lamination and Banding in Sand Injectites: A Cyclic Jamming Model. 63rd British Sedimentological Research Group (BSRG) Annual General Meeting. 16th–18th December 2024 University of Leeds.”

Komar, P. D. 2007. “Chapter 1 the Entrainment, Transport and Sorting of Heavy Minerals by Waves and Currents. Heavy Minerals in Use.” In *Development in Sedimentology*, 3–48. Elsevier. https://doi.org/10.1016/s0070-4571(07)58001-5.

Linn, A. M., D. J. DePaolo, and R. V. Ingersoll. 1992. “Nd–Sr Isotopic, Geochemical, and Petrographic Stratigraphy and Paleotectonic Analysis: Mesozoic Great Valley Forearc Sedimentary Rocks of California.” *Geological Society of America Bulletin* 104: 1264–1279. https://doi.org/10.1130/0016-7606.

Lonergan, L., N. Lee, H. D. Johnson, J. A. Cartwright, and R. J. H. Jolly. 2000. “Remobilization and Injection in Deepwater Depositional Systems: Implications for Reservoir Architecture and Prediction.” In *Deep-Water Reservoirs of the World. GCSSEPM Foundation, 20th Annual Conference*, edited by P. Weimer, R. M. Slatt, and D. T. Lawrence, 515–532. Society of Economic Paleontologists and Mineralogists.

Luzinski, W. M., A. C. Morton, and A. Hurst. 2025. “Sand Injection or Deposition: A Perspective From Mineral-Chemical Stratigraphy.” *Basin Research* 37, no. 5: 1–18. https://doi.org/10.1111/bre.70063.

Luzinski, W. M., A. C. Morton, A. Hurst, I. I. Tøllefsen, and J. Cater. 2022. “Provenance Variability in Coeval Slope Channel Systems: Hermod S2 Member Sandstone (Eocene), South Viking Graben (North Sea).” *Geosciences* 12, no. 12: 450. https://doi.org/10.3390/geosciences12120450.

MacLeod, M. K., R. A. Hanson, C. R. Bell, and S. McHugo. 1999. “The Alba Field Ocean Bottom Cable Seismic Survey: Impact on Development.” *Leading Edge* 18, no. 11: 1306–1312. https://doi.org/10.1190/1.1438206.

Mange, M. A., and D. T. Wright. 2007. “High-Resolution Heavy Mineral Analysis (HRMA): A Brief Summary.” In *Developments in Sedimentology*, edited by M. A. Mange and D. T. Wright, vol. 58, 433–436. Elsevier.

Mange-Rajetzky, M. A. 1995. "Subdivision and Correlation of Monotonous Sandstone Sequences Using High-Resolution Heavy Mineral Analysis, a Case Study: The Triassic of the Central Graben." In *Non-Biostratigraphical Methods of Dating and Correlation: Geological Society of London*, edited by R. E. Dunay and E. A. Hailwood, vol. 89, 23–30. Special Publication.

Martín-Fernández, J. A., C. Barceló-Vidal, and V. Pawlowsky-Glahn. 2003. "Dealing With Zeros and Missing Values in Compositional Data Sets Using Nonparametric Imputation." *Mathematical Geology* 35, no. 3: 253–278.

McElreath, R. 2020. *Statistical Rethinking: A Bayesian Course With Examples in R and Stan*. 2nd ed. CRC Press.

McGuire, D. J. 1988. "Stratigraphy, Depositional History, and Hydrocarbon Source-Rock Potential of the Upper Cretaceous–Lower Tertiary Moreno Formation, Central San Joaquin Basin, California. Doctoral Thesis, Stanford University, CA."

Milam, R. 1985. "Biostratigraphy and Sedimentation of the Eocene and Oligocene Kreyenhagen Formation, Central California." pp. 1–240.

Mitchell, C., S. A. Graham, and D. H. Suek. 2010. "Subduction Complex Uplift and Exhumation and Its Influence on Maastrichtian Forearc Stratigraphy in the Great Valley Basin, Northern San Joaquin Valley, California." *Bulletin of the Geological Society of America* 122: 2063–2078. https://doi.org/10.1130/B30180.1.

Morton, A. 2012. "Value of Heavy Minerals in Sediments and Sedimentary Rocks for Provenance, Transport History and Stratigraphic Correlation." Mineralogical Association of Canada Short Course 42, St. John's NL. pp. 133-165.

Morton, A. C. 1985. "Provenance of Arenites." In *Heavy Minerals in Provenance Studies*, vol. 249–277. Springer Netherlands. https://doi.org/10.1007/978-94-017-2809-6_12.

Morton, A. C., and C. Hallsworth. 1994. "Identifying Provenance-Specific Features of Detrital Heavy Mineral Assemblages in Sandstones." *Sedimentary Geology* 90, no. 3–4: 241–256. https://doi.org/10.1016/0037-0738(94)90041-8.

Morton, A. C., and C. R. Hallsworth. 1999. "Processes Controlling the Composition of Heavy Mineral Assemblages in Sandstones." *Sedimentary Geology* 124: 3–29. https://doi.org/10.1016/S0037-0738(98)00118-3.

Morton, A. C., and A. Hurst. 1995. "Correlation of Sandstones Using Heavy Minerals: An Example From the Statfjord Formation of the Snorre Field, Northern North Sea." In *Non-Biostratigraphical Methods of Dating and Correlation: Geological Society of London*, edited by R. E. Dunay and E. Hailwood, vol. 89, 3–22. Lyell.

Morton, A. C., S. McFadyen, A. Hurst, J. Pyle, and P. Rose. 2014. "Constraining the Origin of Reservoirs Formed by Sandstone Intrusions: Insights From Heavy Mineral Studies of the Eocene in the Forties Area, U.K. Central North Sea." *American Association of Petroleum Geologists Bulletin* 98: 545–561.

Moxon, I. W., and S. A. Graham. 1987. "History and Controls of Subsidence in the Late Cretaceous-Tertiary Great Valley Forearc Basin, California." *Geology* 15: 626–629.

Nilsen, T. H., T. W. J. Dibblee, and T. R. J. Simoni. 1974. "Stratigraphy and Sedimentology of the Cantua Sandstone Member of the Lodo Formation, Vallecitos Area, California." U.S. Geological Survey. SEPM Pacific Section Volume and Guidebook, pp. 38–68.

Palladino, G., G. I. Alsop, A. Grippa, G. Zvirtes, R. P. Phillip, and A. Hurst. 2018. "Sandstone-Filled Normal Faults: A Case Study From Central California." *Journal of Structural Geology* 110: 86–101. https://doi.org/10.1016/j.jsg.2018.02.013.

Palladino, G., A. Grippa, D. Bureau, G. Ian, and A. Hurst. 2016. "Emplacement of Sandstone Intrusions During Contractional Tectonics." *Journal of Structural Geology* 89: 230–249. https://doi.org/10.1016/j.jsg.2016.06.010.

Palladino, G., R. Rizzo, G. Zvirtes, et al. 2020. "Multiple Episodes of Sand Injection Leading to Accumulation and Leakage of Hydrocarbons Along the San Andreas/San Gregorio Fault System, California." *Marine and Petroleum Geology* 118: 10.31223/osf.io/g6r8v.

Payne, M. B. 1951. "Type Moreno Formation and Overlying Eocene Strata on the West Side of the San JoaquinValley, Fresno and MercedCounties." California Division of Mines, Geological Special Report, 9.

Pearson, K. 1897. "Mathematical Contributions to the Theory of Evolution. On a Form of Spurious Correlation Which May Arise When Indices Are Used in the Measurement of Organs." *Proceedings of the Royal Society of London* 60: 489–498.

Pelto, C. R. 1954. "Mapping of Multicomponent Systems." *Journal of Geology* 62, no. 2: 151–155.

Poulsen, M. L., H. Friis, J. B. Svendsen, C. B. Jensen, and R. E. Brulin. 2007. "The Application of Bulk Rock Geochemistry to Reveal Heavy Mineral Sorting and Flow Units in Thick, Massive Gravity Flow Deposits, Siri Canyon Palaeogene Sands, Danish North Sea." In *Heavy Minerals in Use*, edited by M. A. Mange and D. T. Wright, vol. 58, 1229–1253. Elsevier.

Ravier, E., M. Guiraud, A. Guillien, E. Vennin, J. F. Buoncristiani, and E. Portier. 2015. "Micro- to Macro-Scale Internal Structures, Diagenesis and Petrophysical Evolution of Injectite Networks in the VocontianBasin (France): Implications for Fluid Flow." *Marine and Petroleum Geology* 64: 125–151. https://doi.org/10.1016/j.marpetgeo.2015.02.040.

Ross, J. A., J. Peakall, and G. M. Keevil. 2014. "Facies and Flow Regimes of Sandstone-Hosted Columnar Intrusions: Insights From the Pipes of Kodachrome Basin State Park." *Sedimentology* 61: 1764–1792.

Scheirer, H. A., and L. B. Magoon. 2008. "Age, Distribution, and Stratigraphic Relationship of Rock Units in the San Joaquin Basin Province, California: Chapter 5 in Petroleum Systems and Geologic Assessment of Oil and Gas in the San Joaquin Basin Province, California. Professional Paper." https://doi.org/10.3133/pp17135.

Schulein, B. J. 1993. "Sedimentation and Tectonics of the Upper Lower to Lower Middle Eocene Domengine Formation Vallecitos Syncline, California." (M.Sc. Thesis), Stanford, California, Stanford University. pp. 343.

Scott, A., A. Hurst, and M. Vigorito. 2013. "Outcrop-Based Reservoir Characterization of a Kilometer-Scale Sand-Injectite Complex." *AAPG Bulletin* 97: 309–343. https://doi.org/10.1306/05141211184.

Scott, A., M. Vigorito, and A. Hurst. 2009. "The Process of Sand Injection: Internal Structures and Relationships With Host Strata (Yellowbank Creek Injectite Complex, California, U.S.A.)." *Journal of Sedimentary Research* 79: 568–583. https://doi.org/10.2110/jsr.2009.062.

Shannon, C. E. 1948. "A Mathematical Theory of Communication." *Bell System Technical Journal* 27, no. 3: 379–423.

Sharman, G. R., S. A. Graham, M. Grove, and J. K. Hourigan. 2013. "A Reappraisal of the Early Slip History of the San Andreas Fault, Central California, USA." *Geology* 41, no. 7: 727–730.

Sharman, G. R., S. A. Graham, M. Grove, D. L. Kimbrough, and J. E. Wright. 2015. "Detrital Zircon Provenance of the Late Cretaceous-Eocene California Forearc: Infl Uence of Laramide Low-Angle Subduction on Sediment Dispersal and Paleogeography." *Bulletin of the Geological Society of America* 127: 38–60. https://doi.org/10.1130/B31065.1.

Sharman, G. R., T. M. Schwartz, L. E. Shumaker, et al. 2017. "Submarine Mass Failure Within the Deltaic Domengine Formation (Eocene), California (USA)." *Geosphere* 13: 950–973. https://doi.org/10.1130/GES01442.1.

Sherry, T. J., C. D. Rowe, J. D. Kirkpatrick, and E. E. Brodsky. 2012. "Emplacement and Dewatering of the World's Largest Exposed Sand Injectite Complex." *Geochemistry, Geophysics, Geosystems* 13, no. 8: Q08008. https://doi.org/10.1029/2012GC004157.

Snow, C. A., and H. Scherer. 2006. "Terranes of the Western Sierra Nevada Foothills Metamorphic Belt, California: A Critical Review." *International Geology Review* 48, no. 1: 46–62. https://doi.org/10.2747/0020-6814.48.1.46.

Sullivan, R., and M. D. Sullivan. 2012. "Sequence Stratigraphy and Incised Valley Architecture of the Domengine Formation, Black Diamond Mines Regional Preserve and the Southern Sacramento Basin, California, U.S.A: Journal of Sedimentary Research, v. 82, pp. 781–800." https://doi.org/10.2110/jsr.2012.66.

Suppe, J. 1970. "Offset of Late Mesozoic Basement Terrains by the San Andreas Fault System." *Geological Society of America Bulletin* 81, no. 11: 3253.

Surlyk, F., J. Gjelberg, and N. Noe-Nygaard. 2007. "The Upper Jurassic Hareelv Formation of East Greenland: A Giant Sedimentary Injection Complex: Sand Injectites: Implications for Hydrocarbon Exploration and Production." p. 141–149.

Thiel, G. A. 1945. "Mechanical Effects of Stream Transportation in Mineral Grains of Sand Size: Geological Society of America." *Bulletin* 56: 1207.

Todd, T. W., and W. A. Monroe. 1968. "Petrology of Domengine Formation (Eocene), at Potrero Hills and Rio Vista, California." *Journal of Sedimentary Research* 38: 1024–1039. https://doi.org/10.1306/74D71AF0-2B21-11D7-8648000102C1865D.

Unruh, J. R., T. A. Dumitru, and T. L. Sawyer. 2007. "Coupling of Early Tertiary Extension in the Great Valley Forearc Basin With Blueschist Exhumation in the Underlying Franciscan Accretionary Wedge at Mount Diablo, California." *Bulletin of the Geological Society of America* 119: 1347–1367.

Van der Plas, L., and A. C. Tobi. 1965. "A Chart for Judging the Reliability of Point Counting Results." *American Journal of Science* 263, no. 1: 87–90.

Van Oorschot, L. A., J. R. Pyle, G. W. Byerley, and P. T. S. Rose. 2021. "Development of the Brimmond Sand Fairway." In *Subsurface Sand Remobilization and Injection*, edited by S. Silcock, M. Huuse, M. Bowman, A. Hurst, and S. Cobain, vol. 493, 167–180. Geological Society. https://doi.org/10.1144/SP493-2017-350.

Vermeesch, P. 2018. "Statistical Models for Point-Counting Data." *Earth and Planetary Science Letters* 501: 1–7.

Vermeesch, P., G. Resentini, and E. Garzanti. 2016. "An Arctic Perspective on the World's Sandstones: Heavy Mineral Provenance of the Barents Shelf." *Sedimentary Geology* 341: 1–16. https://doi.org/10.1016/j.sedgeo.2016.05.009.

Vigorito, M., A. Grippa, and R. H. T. Callow. 2024. "Controls on the Genesis of a Giant Sand Injection Complex; Insights Into the Paleogene Evolution of the Stress of Northern and Central California." *Journal of the Geological Society* 181, no. 5: 1–25. https://doi.org/10.1144/jgs2024-001.

Vigorito, M., and A. Hurst. 2010. "Regional Sand Injectite Architecture as a Record of Pore-Pressure Evolution and Sand Redistribution in the Shallow Crust: Insights From the Panoche Giant Injection Complex, California." *Journal of the Geological Society* 167: 889–904. https://doi.org/10.1144/0016-76492010-004.

Vigorito, M., A. Hurst, J. A. Cartwright, and A. Scott. 2008. "Regional-Scale Subsurface Sand Remobilization: Geometry and Architecture." *Journal of the Geological Society* 165: 609–612. https://doi.org/10.1144/0016-76492007-096.

Vigorito, M., A. Hurst, A. J. S. Scott, O. Stanzione, and A. Grippa. 2022. "A Giant Sand Injection Complex: Processes and Implications for Basin Evolution and Subsurface Fluid Flow." *American Journal of Science* 322, no. 6: 729–794. https://doi.org/10.2475/06.2022.01.

Wakabayashi, J. 2015. "Anatomy of a Subduction Complex: Architecture of the Franciscan Complex, California, at Multiple Length and Time Scales." *International Geology Review* 57, no. 5–8: 669–746. https://doi.org/10.1080/00206814.2014.998728.

Waltham, R., G. Zvirtes, B. Burnham, and A. Hurst. 2024. "Wing-Like Sandstone Intrusions: Geometric and Spatial Analysis of Outcrop Examples." 63rd British Sedimentological Research Group Annual General Meeting, BSRG 2024, Leeds.

Ward, J. H., Jr. 1963. "Hierarchical Grouping to Optimize an Objective Function." *Journal of the American Statistical Association* 58, no. 301: 236–244. https://doi.org/10.1080/01621459.1963.10500845.

Weltje, G. J. 2002. "Quantitative Analysis of Detrital Modes: Statistically Rigorous Confidence Regions in Ternary Diagrams and Their Use in Sedimentary Petrology." *Earth-Science Reviews* 57, no. 3–4: 211–253.

Weltje, G. J., and H. von Eynatten. 2004. "Quantitative Provenance Analysis of Sediments: Review and Outlook." In *Sedimentary Geology*, edited by G. J. Weltje and H. von Eynatten, vol. 171, 1–11. Elsevier.

Wilson, E. B. 1927. "Probable Inference, the Law of Succession, and Statistical Inference." *Journal of the American Statistical Association* 22, no. 158: 209–212.

Zimmerman, J. 1944. "Tumey Sandstone (Tertiary), Fresno County, California." *Bulletin of the American Association of Petroleum Geologists* 28: 953–976.

Zvirtes, G., A. Hurst, R. P. Philipp, G. Palladino, and A. Grippa. 2019. "The Tumey Giant Injection Complex, Tumey Hill, California (USA)." *Geological Society, London, Special Publications* 493, no. 1: 181–214. https://doi.org/10.1144/sp493-2019-3.

Zvirtes, G., R. P. Philipp, A. Hurst, G. Palladino, L. F. De Ros, and A. Grippa. 2020. "Petrofacies of Eocene Sand Injectites of the Tumey Giant Injection Complex, California (USA)." *Sedimentary Geology* 400: 105617.

Appendix A

TABLE A1 | General information of samples including lithostratigraphy, architecture, injectites and depositional elements, relative depth to Oligocene unconformity and geographic coordinates.

Lithostratigraphy	Sample code	Architecture	Injectite and depositional system	Relative depth	Coordinates	
Tumey Lentil	TL-02	Depositional	Deep marine fan	0	36°36′36.00″ N	120°38′37.87″ W
Kreyenhagen Fm.	UI-53	UII	Dyke (15 cm thick)	10	36°36′22.28″ N	120°38′48.27″ W
	UI-80		Dyke (28 cm thick)	70	36°36′45.41″ N	120°39′7.61″ W
	UI-03		Sill (72 cm thick)	140	36°36′33.40″ N	120°39′24.33″ W
	UI-02		Sill (218 cm thick)	160	36°36′37.68″ N	120°39′21.50″ W
	UI-01		Sill (340 cm thick)	190	36°36′41.88″ N	120°39′20.50″ W
	UI-69		Dyke (50 cm thick)	200	36°36′17.04″ N	120°39′30.12″ W
	UI-129		Sill (86 cm thick)	205	36°36′19.33″ N	120°39′32.83″ W
	UI-87		Dyke (30 cm thick)	230	36°37′29.15″ N	120°39′33.85″ W
	KS-04	UPU	Slope channel-fill (35 m thick)	250	36°37′8.94″ N	120°39′30.80″ W
	KS-06		Slope channel-fill (> 5 m thick)	230	36°36′51.61″ N	120°39′19.33″ W
	LI-62	LII	Sill (25 cm thick)	300	36°36′52.32″ N	120°39′50.42″ W
	LIS104		Sill (20 cm thick)	420	36°36′22.28″ N	120°40′12.06″ W
	LI-101		Sill (160 cm thick)	430	36°36′27.18″ N	120°40′17.30″ W
	LI-105D		Dyke (22 cm thick)	435	36°36′32.25″ N	120°40′29.34″ W
	LI-105C		Dyke (17 cm thick)	438	36°36′32.22″ N	120°40′29.60″ W
	LI-105B		Sill (35 cm thick)	435	36°36′32.02″ N	120°40′29.65″ W
	LI-60		Sill (86 cm thick)	440	36°36′53.68″ N	120°39′55.25″ W
	KS-121	LPU	Slope channels (remobilized)	400	36°36′21.07″ N	120°40′5.25″ W
	KS-119		Slope channels (remobilized)	430	36°36′54.82″ N	120°39′56.91″ W
	KS-99		Slope channels (remobilized)	460	36°36′20.36″ N	120°40′16.74″ W
Domengine Fm.	DS-01	Depositional	Shallow marine sandstone	490	36°36′16.62″ N	120°40′18.02″ W
	DS-132		Shallow marine sandstone	500	36°36′9.02″ N	120°40′7.95″ W
	DS-136		Shallow marine sandstone	510	36°37′42.44″ N	120°40′34.64″ W
Lodo Fm.	LS-05	Depositional	Deep-marine fans	600	36°36′9.59″ N	120°41′2.18″ W
	LS-32		Deep-marine fans	610	36°36′8.67″ N	120°41′2.56″ W

TABLE A2 | Shannon entropy values for mineral assemblage diversity represented in Figure 7B (left diagram).

Architecture	Maen	Median	SD	Count
II	1.71	1.726	0.338	15
Kreyenhagen	1.814	1.896	0.238	5
Domengine (dep.)	2.068	2.088	0.229	3
Lodo (dep.)	1.55	1.55	0.113	2

TABLE A3 | Shannon entropy values for mineral assemblage diversity represented in Figure 7B (right diagram).

Architecture	Mean	Median	SD	Count
UII	1.485	1.506	0.251	8
Kreyenhagen (UPU)	1.604	1.604	0.26	2
LII	1.967	2.023	0.221	7
Kreyenhagen (LPU)	1.955	1.932	0.073	3
Domengine (dep.)	2.068	2.088	0.229	3
Lodo (dep.)	1.55	1.55	0.113	2

TABLE A4 | Aitchison distance matrix values represented in Figure 7C (left diagram).

Architecture	II	Kreyenhagen	Domengine (dep.)	Lodo (dep.)
II	0	2.935549189	5.160607318	3.987510351
Kreyenhagen	2.935549	0	5.695442223	3.50962464
Domengine (dep.)	5.160607	5.695442223	0	5.04524557
Lodo (dep.)	3.98751	3.50962464	5.04524557	0

TABLE A5 | Aitchison distance matrix values represented in Figure 7C (right diagram).

Architecture	UII	UPU	LII	LPU	Domengine (dep.)	Lodo (dep.)
UII	0	3.092866753	2.898787813	3.310846184	5.632813032	3.297387522
Kreyenhagen (UPU)	3.092867	0	3.028010651	2.43162275	4.723843789	2.765219331
LII	2.898788	3.028010651	0	2.757548316	4.192357685	3.693629527
Kreyenhagen (LPU)	3.310846	2.43162275	2.757548316	0	5.435141325	3.193660217
Domengine (dep.)	5.632813	4.723843789	4.192357685	5.435141325	0	5.04524557
Lodo (dep.)	3.297388	2.765219331	3.693629527	3.193660217	5.04524557	0

TABLE A6 | Bayesian statistical analysis of provenance sensitive indices represented in Figure 8A–D.

	Indices																			
	ATi				GZi				RuZi				MZi				CZi			
Architecture	**Mean %**	**Median %**	**Lower CI (90%)**	**Upper CI (90%)**	**Mean %**	**Median %**	**Lower CI (90%)**	**Upper CI (90%)**	**Mean %**	**Median %**	**Lower CI (90%)**	**Upper CI (90%)**	**Mean %**	**Median %**	**Lower CI (90%)**	**Upper CI (90%)**	**Mean %**	**Median %**	**Lower CI (90%)**	**Upper CI (90%)**
Tumey Lentil	92.33	92.81	87.20	97.80	36.38	36.31	30.08	42.75	5.68	5.42	2.13	9.05	5.68	5.42	2.13	9.05	0.95	0.68	0.00	2.15
UII (Dyke)	60.63	60.67	55.70	65.60	29.95	29.87	27.42	32.51	10.72	10.67	8.62	12.69	2.82	2.78	1.61	3.76	1.53	1.49	0.75	2.32
UII (Sill)	39.47	39.43	35.36	44.15	24.58	24.57	22.01	27.17	10.70	10.63	8.76	12.56	2.61	2.58	1.55	3.53	0.97	0.92	0.41	1.61
Kreyenhagen (UPU)	70.74	70.89	64.79	77.55	40.65	40.57	36.78	44.76	6.21	6.12	4.05	8.33	4.17	4.02	2.48	6.10	1.00	0.88	0.21	1.86
LII (Sill)	74.00	74.08	69.99	77.93	42.82	42.82	40.08	45.61	11.24	11.17	8.94	13.35	2.84	2.75	1.71	3.99	1.37	1.31	0.56	2.15
LII (Dyke)	69.29	69.32	65.04	73.89	42.97	42.95	39.92	46.26	9.03	8.90	6.84	11.28	2.85	2.77	1.52	4.14	5.88	5.80	3.96	7.75
Kreyenhagen (LPU)	84.20	84.27	81.20	86.99	48.20	48.21	45.24	51.71	9.03	8.90	6.84	11.28	4.29	4.22	2.72	5.75	1.93	1.87	0.87	2.94
Domengine (dep.)	61.69	61.75	57.56	66.01	54.43	54.47	51.24	57.82	6.88	6.80	4.88	8.78	0.25	0.18	0.00	0.60	3.28	3.21	1.87	4.74
Lodo (dep.)	22.57	22.52	18.01	27.61	34.54	34.59	30.76	38.04	7.94	7.87	5.77	9.89	0.95	0.89	0.28	1.66	0.74	0.67	0.12	1.33

TABLE A7 | Bayesian statistical analysis of provenance sensitive minerals represented in Figure 8E,F. Blueschist minerals (Lawsonite + Glaucophane); Metasediment minerals (Andalusite + Kyanite + Staurolite).

	Blueschist minerals				Metasediments			
Architecture	**Mean %**	**Median %**	**Lower CI (90%)**	**Upper CI (90%)**	**Mean %**	**Median %**	**Lower CI (90%)**	**Upper CI (90%)**
Tumey Lentil (dep.)	0.512	0.354	0.000	1.151	0.961	0.813	0.022	1.928
UII (Dyke)	0.761	0.714	0.291	1.233	5.244	5.182	4.010	6.586
UII (Sill)	0.859	0.813	0.365	1.349	6.164	6.103	4.829	7.606
Kreyenhagen (UPU)	0.957	0.896	0.255	1.629	2.734	2.658	1.415	3.996
LII (Sill)	0.490	0.452	0.118	0.840	5.244	5.182	4.010	6.586
LII (Dyke)	4.136	4.088	2.893	5.480	4.826	4.783	3.387	6.106
Kreyenhagen (LPU)	1.663	1.603	0.753	2.478	4.455	4.401	3.084	5.787
Domengine (dep.)	17.070	17.064	14.555	19.460	1.510	1.446	0.633	2.264
Lodo (dep.)	0.756	0.670	0.139	1.418	1.736	1.635	0.733	2.797

TABLE A8 | Principal Component Analysis of index centroids (Bayesian medians) represented in Figure 9B.

	Indices																			
	ATi				**GZi**				**RuZi**				**MZi**				**CZi**			
Architecture	**Mean %**	**Median %**	**Lower CI (90%)**	**Upper CI (90%)**	**Mean %**	**Median %**	**Lower CI (90%)**	**Upper CI (90%)**	**Mean %**	**Median %**	**Lower CI (90%)**	**Upper CI (90%)**	**Mean %**	**Median %**	**Lower CI (90%)**	**Upper CI (90%)**	**Mean %**	**Median %**	**Lower CI (90%)**	**Upper CI (90%)**
II	60.654	60.680	58.292	62.625	34.741	34.768	33.406	36.063	10.382	10.359	9.342	11.413	2.665	2.649	2.121	3.256	2.102	2.087	1.617	2.666
Kreyenhagen (PU)	80.678	80.740	77.890	83.358	45.365	45.313	42.871	47.853	7.753	7.728	6.215	9.413	4.068	4.032	2.884	5.162	1.421	1.381	0.683	2.118
Domengine (dep.)	61.692	61.754	57.559	66.012	54.428	54.466	51.239	57.816	6.883	6.800	4.876	8.781	0.251	0.177	0.001	0.598	3.283	3.206	1.866	4.737
Lodo (dep.)	22.566	22.519	18.007	27.607	34.540	34.593	30.758	38.040	7.941	7.874	5.775	9.891	0.950	0.885	0.284	1.661	0.743	0.668	0.116	1.329

TABLE A9 | Standardized Euclidian Distances for Provenance Similarity Matrix presented in Figure 9C and Dendrogram in Figure 9D.

Architecture	Tumey Lentil (dep.)	Intrusive intervals (II)	Kreyenhagen (PU)	Domengine (dep.)	Lodo (dep.)
Tumey Lentil (dep.)	0.000	3.922	2.165	4.708	4.061
II	3.922	0.000	2.499	3.775	2.818
Kreyenhagen	2.165	2.499	0.000	3.152	3.325
Domengine (dep.)	4.708	3.775	3.152	0.000	4.104
Lodo (dep.)	4.061	2.818	3.325	4.104	0.000

TABLE A10 | ZTR, ZTi and ATi values with Wilson's 90% confidence intervals for lower and upper parent units (LPU and UPU) and lower and upper intrusive intervals (LII and UII) represented in Figure 10.

Sample	Architecture	ZTi_ value	ZTi_Lower CI (90%)	ZTi_Upper CI (90%)	ZTi_ Total	ZTR_ value	ZTR_ Lower CI (90%)	ZTR_ Upper CI (90%)	ZTR_ Total	ATi_ value	ATi_Lower CI (90%)	ATi_Upper CI (90%)	ATi_ Total
UI-53	UII	97.0	92.729	98.8	100	15.0	11.316	19.619	200	95.0	90.084	97.545	100
UI-80	UII	93.0	87.574	96.2	100	11.0	7.868	15.173	200	3.3	0.747	13.640	30
UI-87	UII	66.0	57.878	73.3	100	5.5	3.394	8.794	200	61.0	52.789	68.632	100
UI-69	UII	87.0	80.481	91.6	100	16.5	12.636	21.259	200	0.0	0.000	6.814	37
UI-129	UII	95.0	90.084	97.5	100	64.5	58.775	69.838	200	13.0	5.335	28.531	23
UI-03	UII	86.0	79.341	90.8	100	73.0	67.555	77.831	200	1.0	0.223	4.358	100
UI-02	UII	95.0	90.084	97.5	100	10.5	7.447	14.608	200	51.0	42.860	59.087	100
UI-01	UII	90.0	83.964	93.9	100	10.0	7.027	14.041	200	78.0	70.499	84.026	100
KS-06	UPU	98.0	94.135	99.3	100	22.5	18.029	27.705	200	62.2	49.962	73.096	45
KS-04	UPU	87.0	80.481	91.6	100	18.5	14.415	23.426	200	76.0	68.350	82.281	100
LI-62	LII	95.0	90.084	97.5	100	35.0	29.686	40.714	200	13.8	6.347	27.419	29
LI104	LII	78.0	70.499	84.0	100	20.0	15.762	25.039	200	69.0	60.976	76.023	100
LI-101	LII	67.0	58.907	74.2	100	8.5	5.785	12.323	200	78.0	70.499	84.026	100
LI-105D	LII	84.0	77.087	89.1	100	24.0	19.401	29.293	200	81.0	73.764	86.603	100
LI-105C	LII	78.0	70.499	84.0	100	16.0	12.194	20.713	200	51.0	42.860	59.087	100
LI-105B	LII	90.0	83.964	93.9	100	18.5	14.415	23.426	200	76.0	68.350	82.281	100
LI-60	LII	87.0	80.481	91.6	100	10.0	7.027	14.041	200	93.0	87.574	96.161	100
KS-121	LPU	80.0	72.670	85.7	100	15.0	11.316	19.619	200	87.0	82.590	90.423	200
KS-119	LPU	82.0	74.865	87.4	100	18.0	13.968	22.886	200	83.0	75.972	88.289	100
KS-99	LPU	85.0	78.210	89.9	100	29.0	24.030	34.530	200	80.0	72.670	85.750	100